

Bayesian inference of antibody evolutionary dynamics using multitype branching processes

Athanasios G. Bakis¹, Ashni A. Vora², Tatsuya Araki², Tongqiu Jia³, Jared G. Galloway⁴, Chris Jennings-Shaffer⁴, Gabriel D. Victora^{2,5}, Yun S. Song⁶, William S. DeWitt^{3,4*}, Frederick A. Matsen IV^{4,3,7,5*}, Volodymyr M. Minin^{1*}

1 Department of Statistics, University of California, Irvine, CA, USA

2 Laboratory of Lymphocyte Dynamics, The Rockefeller University, New York, NY, USA

3 Department of Genome Sciences, University of Washington, Seattle, WA, USA

4 Computational Biology Program, Fred Hutchinson Cancer Research Center, Seattle, WA, USA

5 Howard Hughes Medical Institute, Seattle, WA, USA

6 Department of Electrical Engineering & Computer Sciences, University of California, Berkeley, CA, USA

7 Department of Statistics, University of Washington, Seattle, WA, USA

* co-corresponding authors (wsdewitt@uw.edu, matsen@fredhutch.org, vminin@uci.edu)

Abstract

When our immune system encounters foreign antigens (i.e., from pathogens), the B cells that produce our antibodies undergo a cyclic process of proliferation, mutation, and selection, improving their ability to bind to the specific antigen. Immunologists have recently developed powerful experimental techniques to investigate this process in mouse models. In one such experiment, mice are engineered with a monoclonal B-cell precursor and immunized with a model antigen. B cells are sampled from sacrificed mice after the immune response has progressed, and the mutated genetic loci encoding antibodies are sequenced. This experiment allows parallel replay of antibody evolution, but produces data at only one time point; we are unable to observe the evolutionary trajectories that lead to optimized antibody affinity in each mouse. To address this, we model antibody evolution as a multitype branching process and integrate over unobserved histories conditioned on phylogenetic signal in sequence data, leveraging parallel experimental replays for parameter inference. We infer the functional relationship between B-cell fitness and antigen binding affinity in a Bayesian framework, equipped with an efficient likelihood calculation algorithm and Markov chain Monte Carlo posterior approximation. In a simulation study, we demonstrate that a sigmoidal relationship between fitness and binding affinity can be recovered from realizations of the branching process. We then perform inference for experimental data from 52 replayed B-cell lineages sampled 15 days after immunization, yielding a total of 3,758 sampled B cells. The recovered sigmoidal curve indicates that the fitness of high-affinity B cells is over six times larger than that of low-affinity B cells, with a sharp transition from low to high fitness values as affinity increases.

Introduction

Scientific background and problem formulation

Understanding of the adaptive immune system is critical for developing new strategies to fight disease (for example, in immunotherapy and vaccine development) [39]. The antibody-mediated component of the adaptive immune system is carried out by B cells, which produce antibodies. When antibodies are bound to the membrane of a B cell, they are called B cell receptors (BCRs). The BCR is determined by its genetic sequence encoded in the immunoglobulin heavy and light chain loci. An *antigen* is a foreign molecule that is the target of the adaptive immune system; it could be a part of a pathogen or a vaccine. BCRs improve their binding ability to a given antigen during *affinity maturation*, a process that happens in lymph node structures called *germinal centers*.

What mechanistic details do we currently know about affinity maturation? During affinity maturation, B cells compete to optimize the antibody supply for a particular target in a cyclic two-step process, alternating between the so-called *light zone* and *dark zone* of a germinal center [38].

1. **Selection:** B cells compete via their BCRs in the light zone to bind to the antigen; the binding *affinity* is a quantitative measure of binding ability defined in terms of a chemical dissociation constant K_D (having units of molar concentration, with lower values corresponding to higher affinity). B cells that succeed in binding antigen present antigen-derived peptides to and receive signals from T cells that trigger them to migrate to the dark zone and initiate proliferation.
2. **Mutation:** B cells proliferate in the dark zone, mutating the immunoglobulin loci along the way to create new B cells with new, potentially improved BCRs. These cells then migrate back to the light zone.

By some estimates, the rate of mutation in the immunoglobulin loci is six orders of magnitude larger than the genome-wide rate [20, 32]. Consequently, the immune response sees substantial B cell evolution in only a few weeks.

There is a distinction, however, between the affinity of a B cell’s BCRs, and its fitness (cellular proliferation rate) in the affinity maturation process. BCR affinity is a molecular phenotype that can be measured experimentally outside the context of the germinal center. However, fitness—thought to be a function of binding affinity—cannot easily be measured directly in the germinal center. The functional relationship between binding affinity and fitness is therefore not well-characterized quantitatively. For example, there may exist a threshold of binding affinity that is sufficient for proliferative signals from T cells, and any B cells whose BCRs exceed this threshold have the same fitness [3]. Thus, in this paper, we pose the question: what is the functional relationship between the binding affinity of an antibody and the fitness of the B cell that produces it?

Current experiments cannot directly interrogate the extent to which binding affinity determines B cell fitness, as this would require longitudinal sampling of germinal center B cells; current technology can only sample cells after sacrificing the model organism. We opt to develop a likelihood-based statistical method equipped with the ability to handle the unobservable quantities governing affinity maturation, allowing us to learn about this fundamental affinity-fitness relationship without needing to measure it directly. We apply our methodology to a novel experimental dataset of cross-sectional B cell samples from individual germinal centers.

The recent work of DeWitt, Vora, Taraki et al. (2025) provides us with this experimental data [9]. In a highly controlled system, engineered monoclonal B cells specific for the model antigen chicken gammaglobulin (chIgY) were allowed to affinity mature in response to immunization with their cognate antigen. Individual germinal centers from several mice were micro-dissected, and immunoglobulin loci were sequenced.

It is excitingly rare to observe numerous parallel replications of an evolutionary process, as macroevolutionary studies can only observe one replication of most evolutionary events of interest. As stated earlier, longitudinal observation of a germinal center is currently infeasible, as sampling cells is destructive to the germinal center (and the mouse) and terminates affinity maturation; thus, this experiment is cross-sectional in nature. However, we show that, under certain assumptions, control of the germinal center’s initial state is sufficient to infer the affinity-fitness relationship using only a single time point from each replicate.

Related work

From a mathematical modeling point of view, continuous-time branching processes are a classic model for cell division and form a natural basis for our work. These models are parameterized in terms of the rates at which lineages are born or die, and allow us to model the unobserved intermediate evolutionary history of the B cells. We can interpret the rate of birth of a lineage as the fitness of the cell it represents.

Likelihood-based inference for partially-observed branching processes has a long history. Nee et al. (1994) describe how to use a branching process to infer evolutionary dynamics when lineages can go extinct and become unobservable, a key component of our scientific problem [28]. More recent literature builds upon this work, introducing branching processes that allow for lineages of different discrete character states—observed or marginalized over—to have different evolutionary dynamics [25, 14, 21, 5]. These models form the foundation of our approach to inferring how properties of B cells (such as BCR binding affinity) map to their birth rate. FitzJohn (2012) furthers this work to allow for a continuous-valued state, evolving according to a diffusion process [13]. Stadler (2013) and MacPherson et al. (2022) provide further reviews of the developments in this literature [35, 24]. Notably, the permission of transitions between states in these models creates analytical intractabilities when deriving the likelihood; numerical methods are consequently used. However, Barido-Sottani et al. (2020) derive an analytical approximation to the multitype branching process likelihood that assumes character states don’t change in unsampled lineages [2].

These methods, as they stand, are not equipped to handle the details of our scientific question. First, we are interested in inferring the parameters of a function relating binding affinity to birth rate. Only FitzJohn (2012) of the aforementioned literature discusses the specification of flexible functional relationships between rates and states, but its use of diffusion processes to model state changes is difficult to integrate with our prior knowledge of B cell mutation rates. Second, our experimental setup provides us with a sample of independent replicates of evolution (across different germinal centers), which requires a careful investigation of how to create a conditional branching process likelihood suitable for our sampling regime. Finally, we will show the analytical approximation of Barido-Sottani et al. (2020) does not hold in our context and introduces biases in inference.

Our contribution

In our work, we extend the current state-of-the-art multitype branching processes by: (1) inferring parameters of a functional relationship between birth rates and lineage attributes (a trait or phenotype assigned to each type); (2) accommodating multiple independent, partially observed realizations of the branching process; (3) demonstrating that conditioning on the observation of at least one lineage is critical for producing valid statistical inference when analyzing multiple realizations of the process; and (4) allowing for a general parameterization of the rates of type change. We provide an efficient implementation of our inferential pipeline, without approximations of the branching process likelihood. We show that the relationship between birth rates and lineage attributes can be recovered in simulation from independent and identically distributed realizations of the branching process, and that some model misspecification still yields partially robust inference. We demonstrate our method’s application to B cell evolution from a real experiment.

Methods

Data and experimental setup

Consider the following experiment. Mice receive an adoptive transfer of genetically identical monoclonal B cells and are then immunized with the antigen these cells target. The genetic sequence common to these B cells is termed the *naive sequence*. Host mice are engineered to be unable to produce germinal centers with their own B cells; thus, the adoptively transferred B cells are the only ones involved in affinity maturation. After a fixed duration of time (on the order of days), B cells are sampled from germinal centers in the mice, and their immunoglobulin genes are sequenced; sequences are then aligned. This experiment is illustrated in Fig 1.

With these sequences, we have observed the results of I parallel replications of affinity maturation, one for each germinal center sampled across the mice. Let G_{ij} be the genetic sequence of the j^{th} B cell sampled from the i^{th} germinal center ($i = 1, \dots, I$), and \mathbf{G}_i be collection of all these sequences for germinal center i .

We are then provided with a predictive model mapping these B cells’ genetic sequences to the binding affinities of their antibodies to the antigen, using a technology called Tite-Seq [1]. Specifically, a library of all single-amino-acid mutations to the naive sequence was constructed, and the change in the log equilibrium dissociation constant ($-\Delta \log_{10} K_D$) of the resulting antibodies were measured. These are then extended to multi-amino-acid mutations using an additive model [9]. Let $A(G_{ij})$ be the $-\Delta \log_{10} K_D$ prediction for the antibodies produced by a B cell with sequence G_{ij} , representing a log fold change between binding affinity of G_{ij} relative to the naive sequence. Abusing notation slightly, we will call this measure of binding affinity by the term *binding affinity* itself, with higher values indicating stronger binding to the antigen.

Problem formulation

Our scientific goal is to infer a mapping from the affinity of a B cell’s antibodies (collected in a set \mathcal{X}) to its fitness in the germinal center. Mathematically, we infer a mapping $\lambda_\phi : \mathcal{X} \rightarrow \mathbb{R}^+$ (parameterized by ϕ) from a B cell’s antibody binding affinity to a $\lambda_\phi(A(G_{ij}))$ which describes fitness (this will be made more precise in the next section). Let us emphasize that

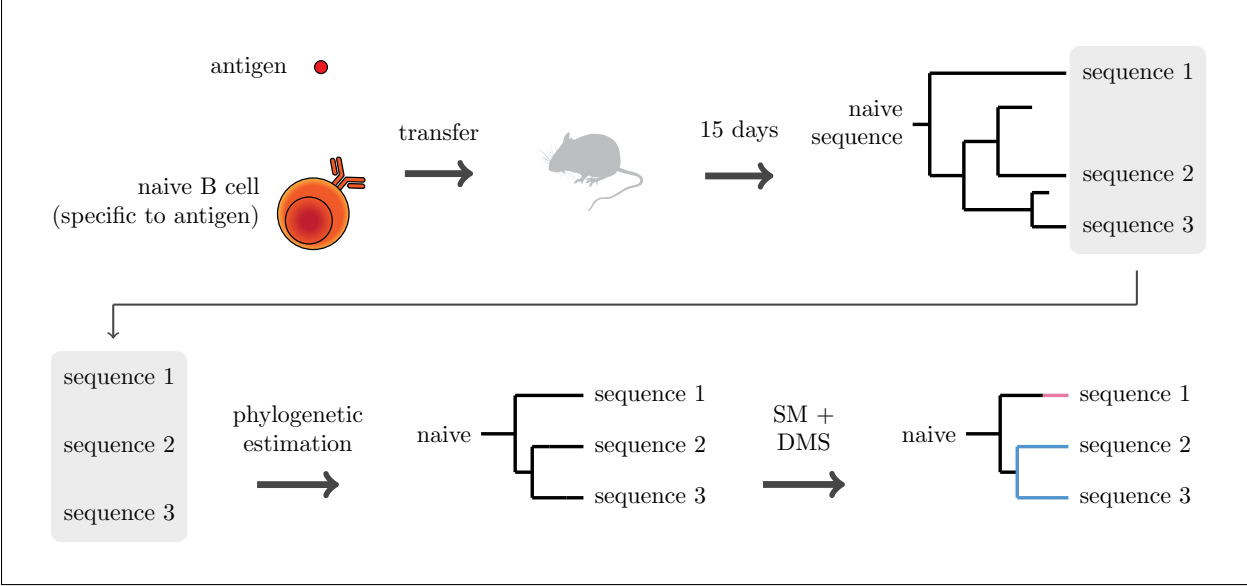


Figure 1: The data-generating experiment. **Top row:** An antigen and B cells are transferred to host mice, initializing affinity maturation. While each germinal center in each mouse experiences a full evolutionary process (represented by the tree), we are unable to observe anything before the present (sampling) time. The sequences at the tips of the tree are all that is collected as data (shaded box). **Bottom row:** Given observed B cell sequences, estimate a phylogenetic tree annotated with mutation times. We then are in the unique position to predict the binding affinity of the antibodies produced by any B cell at any point along the tree, using stochastic mapping (SM) and deep mutational scanning (DMS) data. These inferred and affinity-annotated trees form the input to our model.

there is a fair amount of unobserved data in our experiment, which makes this task challenging. Only a subset of cells alive at the cell collection time are sampled and sequenced; we lack knowledge of any cells that died before collection time or were not sampled. Additionally, the evolutionary history of these cells (sampled or not) is unknown to us.

We will assume, for now, that for each germinal center i , we can use \mathbf{G}_i to estimate T_i , a phylogenetic tree annotated with $A(G)$ for every sequence G at any point on the tree. Example trees observed in this manner are shown in Fig 2. The branch lengths of the tree are measured in units of clock time. The relationship between the number of genetic mutations along a branch and the time elapsed is estimable because of our knowledge of the state of the tree at two distinct time points—the root and tips of the tree [10, 12].

Branching process

We now specify the probability model that relates the phylogenetic tree T_i to our notion of fitness λ_ϕ . Let us first describe the generating process for the tree. We employ a branching process in which individuals of different “types” have different evolutionary dynamics, adopting notation from Barido-Sottani et al. (2020). Assume there is a finite set \mathcal{X} of possible discrete character states (further referred to as *types*), one of which describes an individual at any given point in time. The process begins with a single individual of type $x \in \mathcal{X}$ at time $t = 0$. A continuous-time Markov process is then run, with parameters describing the rates at which the individual either: (1) gives birth to a new individual of the same type, (2) dies, or (3) changes to a different type. Finally, leaves on the tree are marked as sampled according to specified probability parameters (one for survivors, and one for dead lineages), and subtrees without any sampled lineages are pruned away and considered unobserved. Fig 3 illustrates this process. Note that type changes do not occur during birth events, and that there is a separate constant birth rate parameter associated with each type.

This model with type-specific birth rates appears useful to us at first glance, as we can use the birth rates as a proxy for the fitness function λ_ϕ we aim to infer. In this setup, the possible types $x \in \mathcal{X}$ are the binding affinities of the antibodies produced by the B cells (and thus, \mathcal{X} is an ordered set). However, the discrete birth rate setup can become problematic as the size of the type space increases, and in our context, there are hundreds of binding affinities to which fitness values must be assigned. Some existing literature has instead opted to create a continuous type space for the multitype branching process, but models the type change process in a way that is difficult to harmonize with our prior model of B cell mutations [13]. We would like to instead constrain our parameterization in the discrete setup and facilitate information sharing, as well as enable interpolation of the birth rate at types which may not explicitly be in the type space.

Therefore, we build on this notion of type-specific birth rates by replacing the discrete set of birth rates with our choice of parametric curve $\lambda_\phi : \mathcal{X} \rightarrow \mathbb{R}^+$, e.g., a sigmoidal $\lambda_\phi(x) = \phi_1 / [1 + \exp(-\phi_2(x - \phi_3))] + \phi_4$. Now, our branching process still requires that the type space be finite, so we must discretize the range of possible binding affinities to create this type space. We thus still only infer $|\mathcal{X}|$ (the cardinality of the set) birth rates in the branching process, but we constrain them to obey the functional form of λ_ϕ . Our discretization strategy is explained in Section *Discretization of affinity values for type space*.

Notice how the tree realized from this continuous-time Markov process contains more than just the timings of birth events typically seen in a phylogenetic tree. First, there are death events, marking the end of a lineage prior to collection time. In our experimental setup, we are unable to sample a dead cell from the germinal center, and thus are always

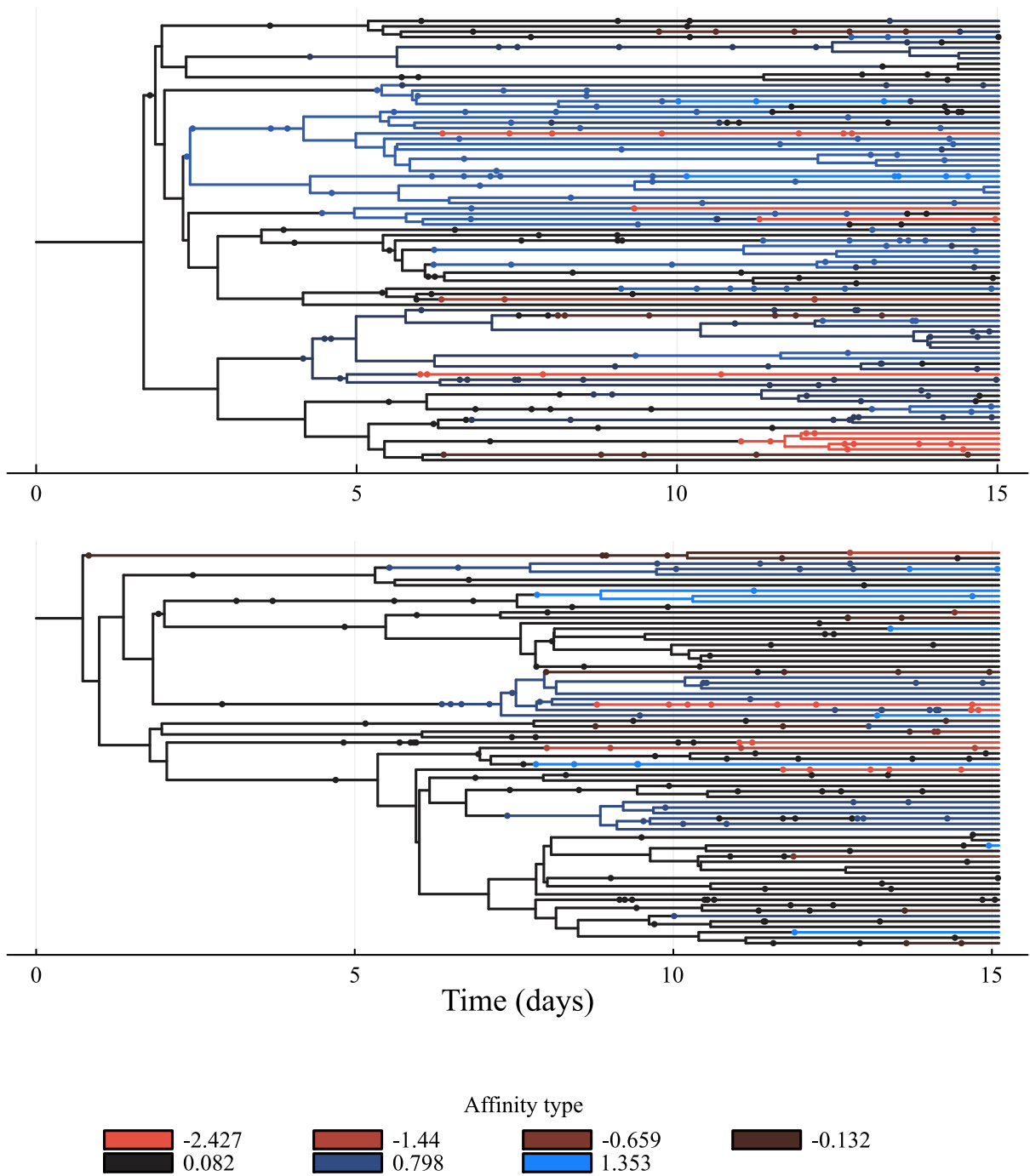


Figure 2: One sampled tree from each of two different germinal centers, as output by BEAST. Branches are colored by discretized affinity value, and dots represent nucleotide-level B cell mutations (including those that do not change the affinity of the antibody).

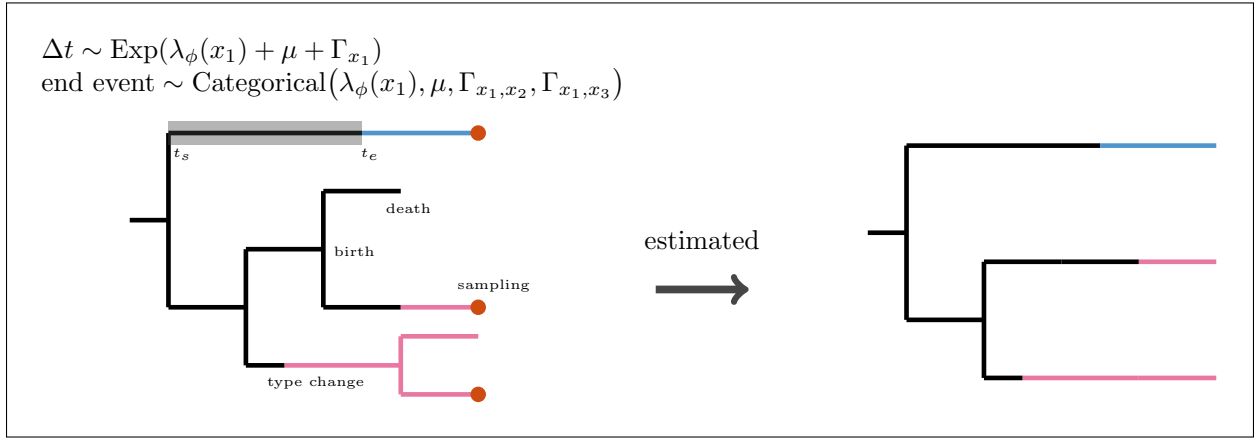


Figure 3: The data-generating process for the branching process. The parameters $\lambda(\cdot), \mu, \Gamma$ correspond to birth, death, and type change rates, respectively. **Left:** Waiting times and events are sampled to create a tree. Categorical distribution probabilities are obtained by normalizing the stated weights, which are written as such in the diagram for brevity. For example, the probability that a segment in type x_1 ends in a birth event is $\lambda_\phi(x_1) / [\lambda_\phi(x_1) + \mu + \Gamma_{x_1,x_2} + \Gamma_{x_1,x_3}]$. Colors represent types; here, black is type x_1 , red is type x_2 , and blue is type x_3 . Lineages which are sampled at collection time are marked with dots on the tips of the tree. The highlighted branch segment is explained by the mathematical captions adjacent to them. **Right:** Information about lineages that died or were not sampled is lost, yielding the tree on observed lineages.

working with trees whose leaves are exclusively survived cells. Our branching process will accommodate this by setting the sampling probability of dead lineages to zero. The tree now also contains type change events, where a cell of one type changes to another. Our types are discretized binding affinities, which we assume we can measure.

Let us now formally derive the density calculation of our branching process, in the spirit of Barido-Sottani et al. (2020). Recall that every point on the tree is annotated with a binding affinity value $A(\cdot)$. Let \mathcal{X} , the type space, be a finite set of numbers corresponding to discretized binding affinity values, for some discretization function. Define the following parameters, which will collectively be referred to as θ :

- ϕ , the parameters which define the birth rate function $\lambda_\phi : \mathcal{X} \rightarrow \mathbb{R}^+$;
- $\mu > 0$, the death rate parameter, chosen to be constant over \mathcal{X} [27];
- Γ , the type change rate matrix of dimension $|\mathcal{X}| \times |\mathcal{X}|$;

Let $\Gamma_{x,x'}$ denote the rate at which a cell of type x changes to type x' for $x \neq x'$.

Let $-\Gamma_{x,x} \stackrel{\text{def}}{=} \Gamma_x \stackrel{\text{def}}{=} \sum_{x' \neq x} \Gamma_{x,x'}$ denote the rate at which a cell of type x changes to any other type.

- ρ , the probability that a cell alive at the collection time is sampled, and thus observed in the tree. (Recall not every cell present in the germinal center will be sampled.)

Note that Barido-Sottani et al. (2020) include a parameter σ for the probability that a dead lineage is sampled for inclusion in the tree. As discussed earlier in this section, we set $\sigma = 0$ to align the branching process with our experimental setup of sampling only living cells.

Our goal is to compute the density $p(T_i|\boldsymbol{\theta})$ for the tree T_i . Recall T_i contains information of both the births and type change events of sampled B cell lineages in germinal center i ; our strategy for annotating type changes is discussed in Section *Data description*. Note that we measure the times $t > 0$ of these events as the duration of time remaining until collection time 0.

Let us first define an auxiliary probability that is useful in computing this density. Let $p_x(t)$ be the probability that a cell with type x at time $t > 0$ is not observed at collection time 0 in the tree, nor are any of its descendants. Following Barido-Sottani et al. (2020), p_x is defined through the following system of ordinary differential equations (over $x \in \mathcal{X}$):

$$\begin{aligned} p_x(0) &= 1 - \rho, \\ \frac{dp_x}{dt}(t) &= -(\lambda_\phi(x) + \mu + \Gamma_x)p_x(t) + \mu + \lambda_\phi(x)p_x(t)^2 + \sum_{x' \neq x} \Gamma_{x,x'}p_{x'}(t). \end{aligned} \quad (1)$$

To assign probability density to the entire tree T_i , we consider how we can aggregate densities of every *segment* N of T_i . A segment is defined as the stretch of tree branch between any two adjacent events: birth, death, or type change. Let $t_{s,N}$ and $t_{e,N} < t_{s,N}$ be the start and end times of branch segment N , respectively. We then let $q_N(t)$, $t \in [t_{e,N}, t_{s,N}]$ be the probability density of the subtree of T beginning with (and including) the portion of tree segment N occurring after time t . As in Barido-Sottani et al. (2020), this quantity is also defined through an ordinary differential equation,

$$\begin{aligned} \frac{dq_N}{dt}(t) &= -(\lambda_\phi(x_N) + \mu + \Gamma_x)q_N(t) + 2\lambda_\phi(x_N)q_N(t)p_{x_N}(t), \quad \text{with initial condition} \\ q_N(t_{e,N}) &= \begin{cases} \rho & \text{if } N \text{ ends in a sampling event at collection time} \\ & t_{e,N} = 0, \\ \lambda_\phi(x_N)q_{N'}(t_{s,N'})q_{N''}(t_{s,N''}) & \text{if } N \text{ ends in a birth event at time } t_{e,N} > 0 \\ & \text{yielding child segments } N' \text{ and } N'', \\ \Gamma_{x_N, x_{N'}}q_{N'}(t_{s,N'}) & \text{if } N \text{ ends in a type change event at time } t_{e,N} > \\ & 0 \text{ yielding segment } N', \end{cases} \end{aligned} \quad (2)$$

where x_N is the type of the cell represented by segment N . Notice how the initial conditions are explicitly defined for the segments that end at leaves in the tree (i.e. sampling events), whereas the initial conditions for the other segments require the values of q of their child segments. By performing a postorder traversal through the tree and computing q during this traversal, we visit every segment in such an order that child segments always have q computed before visiting a parent segment. This traversal ultimately ends at the root segment N_{root} , which begins at time $t_{s, N_{\text{root}}}$. By construction, the value of q for this root segment is the probability density of the entire tree T_i on observed lineages, i.e.,

$$p(T_i|\boldsymbol{\theta}) = q_{N_{\text{root}}}(t_{s, N_{\text{root}}}). \quad (3)$$

Note that exploiting the linearity of the ODE may result in a more efficient implementation; we will consider this in future work.

We have not finished, though, due to the importance of considering a conditional distribution over trees. With the multitype branching process-induced density in Eq (3), any tree T_i is a valid realization of the process—including those where all cells go extinct. However,

in our scientific problem, germinal centers are only sampled if they exist at collection time; our experimental setup has no way of inferring a tree without lineages that survived to the sampling time. If we do not condition on this information, our death rate parameter will be severely underestimated, as it will appear that cells are rarely dying. Stadler (2013) explores conditioned branching process likelihoods further (in the context of the constant rate parameters) and indeed makes the recommendation to condition the model on the survival of at least one sampled lineage [34]. However, this conditioning is not common practice when working with multitype branching processes, possibly because the difference between conditioning and not conditioning is not very pronounced when analyzing only one realization of the process [2]. We will show in the Results that conditioning is important when analyzing multiple trees jointly.

Thus, we condition Eq (3) on the event that the tree T_i produced at least one observed lineage. Fortunately, the probability of this event is easily accessible as a solution of the ODE defined earlier (Eq (1)); it is $p_{x_{\text{root}}}(t_s, N_{\text{root}})$, where x_{root} is the type of the cell at the root of the tree. We ultimately work with the conditional tree density, denoted p_c :

$$p_c(T_i|\boldsymbol{\theta}) = \frac{q_{N_{\text{root}}}(t_s, N_{\text{root}})}{1 - p_{x_{\text{root}}}(t_s, N_{\text{root}})}. \quad (4)$$

Putting it all together

With $\boldsymbol{\theta}$ defined as in Section *Branching process*, our target of inference is:

$$p(\boldsymbol{\theta}|\mathbf{T}) \propto p(\boldsymbol{\theta}) \prod_i p_c(T_i|\boldsymbol{\theta}). \quad (5)$$

Hamiltonian Monte Carlo or any other MCMC, in principle, can be used for this posterior. There are several considerations to make when adapting this methodology to an experiment, though:

1. The functional form of the birth rate $\lambda_\phi : \mathcal{X} \rightarrow \mathbb{R}^+$ needs to be chosen.
2. As described in Section *Branching process*, the interval of possible binding affinities needs to be discretized in some manner to create a type space for the branching process.
3. As discussed by Stadler and Bonhoeffer (2013), there are identifiability concerns around the parameters $\lambda_\phi(\cdot), \mu, \rho$ [36]. One solution is to fix one of the parameters (often ρ) using prior information. Alternatively, we hypothesize that setting a highly informative prior distribution on one of the parameters is sufficient.
4. The matrix $\mathbf{\Gamma}$ can be inferred in principle, but given prior information about B cell mutation dynamics, it may be preferable to fix this parameter and greatly reduce the overall number of inferred quantities. One approach is to replace $\mathbf{\Gamma}$ in the branching process with the term $\delta\mathbf{\Gamma}^*$, where $\mathbf{\Gamma}^*$ is the known prior-informed rate matrix, and δ is an unknown scalar parameter to be inferred jointly with other model parameters.

We discuss our own decisions for these points (in relation to our experimental data) in Section *Adapting our methodology to the experimental setup of DeWitt, Vora, Taraki et al. (2025)*.

Our implementation

Bayesian inference was conducted via Hamiltonian Monte Carlo with No-U-Turn Sampling in the Julia programming language using the Turing probabilistic programming library [6, 19, 15]. Our package implementing a tree simulator and density computation for branching process can be found at <https://github.com/thanasibakis/gcdyn.jl>. The numerical integration for density computation was conducted using the DifferentialEquations.jl package [30]. Our package implementing additional tree simulators and B cell mutation models (for examining robustness to model misspecifications) can be found at <https://github.com/matsengrp/gcdyn>. Our code for the following data analyses and simulation studies can be found at <https://github.com/thanasibakis/gcdyn-analyses>.

Results

Adapting our methodology to the experimental setup of DeWitt, Vora, Taraki et al. (2025)

We now address our modeling decisions for the considerations discussed in Section *Putting it all together*.

1. The birth rate function is specified to have a sigmoidal form, $\lambda_\phi(x) = \phi_1 / \{1 + \exp[-\phi_2(x - \phi_3)]\} + \phi_4$.
2. We examine genetic sequences from a separate experiment to form our type space; see Section *Discretization of affinity values for type space* below.
3. We use prior knowledge to fix ρ . Specifically, in simulation studies, we assume ρ is known (unless otherwise stated), and in data analysis, we fix individual germinal center-specific parameters estimated as $\rho_i = \frac{|G_i|}{1000}$, i.e., the observed number of cells in the germinal center divided by the prior-informed total number of cells at time of sampling.
4. We use prior knowledge to fix Γ and introduce a scalar δ alongside it; see Section *A priori estimation of type change rate matrix* below.

Thus, the parameters we infer in Eq 5 are $\theta = (\phi, \mu, \delta)$. The details of some of these decisions here are given below.

Discretization of affinity values for type space

We now describe how we discretize the continuous range of affinity values we observe in our tree samples. Naively, we may propose to collect all observed affinity values in both the leaf and ancestral tree nodes across the 52 germinal centers, and create n bins from evenly-spaced cutoff values. We can then use the median affinity within the bin to be the representative type value for that bin. However, there may be a bias with this technique; we may observe fewer instances of small binding affinities, since the B cells producing those antibodies would likely not be selected for in the affinity maturation process and thus would not survive.

As a result, we instead use a second set of data from the 10X Genomics platform, which contains BCR sequences sampled from mice sacrificed at different points in time during the

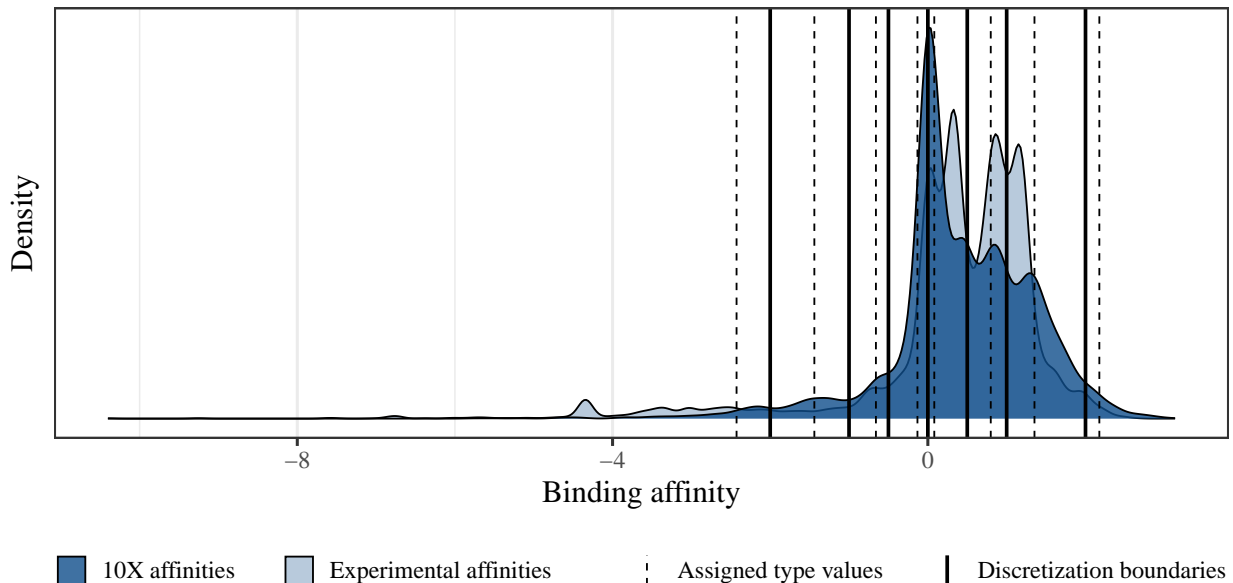


Figure 4: Density plots of the binding affinities seen in the 10X data and from one tree sample for each germinal center in our experimental dataset. The boundaries of the bins used to create the type space are marked in black. Type values (bin medians) are represented by dashed lines. Any affinities in our experimental dataset that lie outside the extreme boundaries are assigned to the extreme bins.

affinity maturation process [9]. The difference between this 10X data and the original data is that the former does not track to which germinal center each B cell belongs. We use the affinity values from these sequences to determine the bin values for our discretization. Choosing $n = 8$, we obtain $\mathcal{X} = [-2.43, -1.44, -0.66, -0.13, 0.08, 0.8, 1.35, 2.18]$. An illustration of the type space created from this discretization, as well as its juxtaposition to the affinities observed in our experimental dataset, is shown in Fig 4.

A priori estimation of type change rate matrix

We now discuss our prior knowledge of the rates of change between the types in our type space. Previous work has yielded a hotspot-aware model of nucleotide-level mutations in B cell sequences [40, 7]. We developed a simulator that, given a B cell receptor sequence, runs a continuous-time Markov process over sequences for a fixed amount of time ($t = 200$, with a mutation rate of 1), initialized to the given sequence and transitioning between sequences according to this context-dependent mutation model. The simulator outputs a chain of sampled mutations that occur; no birth or death events are permitted. The resulting mutations can then be mapped to the corresponding discretized affinity values. Finally, we can compute the maximum likelihood rate of change between each pair of affinity values using the frequencies of each transition observed in simulation.

A rate matrix inferred this way from our experimental dataset, however, would be biased by the selection process in the germinal center, similarly to the discretization problem discussed earlier. Instead, we opt to apply this simulator to the 5,520 sequences observed in the 10X data during the timeframe of 5 to 20 days after germinal center initialization. The

resulting rate matrix, to three decimal places, is:

$$\Gamma = \frac{1}{1000} \begin{pmatrix} -4.62 & 3.35 & 0.45 & 0.27 & 0.36 & 0.09 & 0.09 & 0.0 \\ 202.08 & -220.91 & 13.88 & 3.17 & 0.99 & 0.2 & 0.59 & 0.0 \\ 110.3 & 150.73 & -288.49 & 22.63 & 4.61 & 0.22 & 0.0 & 0.0 \\ 92.16 & 51.13 & 98.46 & -285.71 & 36.19 & 7.77 & 0.0 & 0.0 \\ 86.54 & 24.62 & 65.35 & 132.85 & -332.07 & 18.27 & 4.44 & 0.0 \\ 72.06 & 21.89 & 15.3 & 48.68 & 100.97 & -283.56 & 24.66 & 0.0 \\ 58.28 & 20.7 & 7.92 & 13.29 & 48.06 & 99.69 & -253.06 & 5.11 \\ 64.6 & 29.82 & 9.94 & 9.94 & 9.94 & 14.91 & 168.96 & -308.11 \end{pmatrix}$$

This rate matrix is not necessarily on the same timescale as the data we analyze, as the configuration of the Markov process mutation rate here was arbitrary. We therefore create a scaling parameter δ to be inferred, and use $\delta\Gamma$ as the type change rate matrix in the branching process.

Simulation studies

Importance of a conditional model

Before evaluating our methodology in simulation, we first demonstrate the importance of using the conditional density in Eq (4). Consider a simple single-type branching process with constant birth rate $\lambda_\phi(\cdot) = 1.8$ and death rate $\mu = 1$, where all surviving lineages are sampled ($\rho = 1$). Suppose we have a rejection sampling algorithm that samples trees from this process, but only accepts trees where the number of lineages alive at collection time is at least 1. Using this sampler, we generate 100 sets of n trees each. For each tree set, we then run Metropolis-Hastings sampling within Gibbs, targeting the posterior,

$$p(\lambda, \mu | \mathbf{T}) \propto p(\lambda, \mu) \prod_i p_c(T_i | \lambda, \mu), \quad (6)$$

with log-normal proposals for λ and μ and likelihood as in Eq (4), and retain posterior medians for the two rate parameters. A log-normal(1.5, 1) prior is used for λ , and a log-normal(0, 0.5) prior is used for μ .

The goal here is to compare the sampling distributions of the posterior median rates under this conditioned model to the corresponding distributions obtained if the unconditioned model is used, so we also run this procedure targeting the posterior for the unconditioned likelihood as in Eq (3). This experiment is then repeated for different sample sizes n to further understand the effects of the choice of likelihood.

This experiment clearly demonstrates that the conditioned model mitigates a bias present when using the unconditioned model (Fig 5). For $n = 1$, as is typical in a macroevolutionary context, we may not notice the minimal bias present by using an unconditioned tree model. However, as the number of trees sampled increases, the bias becomes more apparent, as shown in Fig 5. We further note that the bias is especially extreme for the death rate parameter; the unconditioned model will tend to severely underestimate the death rate, since it will appear that cells are rarely dying.

Birth rate recovery, no model misspecification

We now demonstrate the performance of our inferential method in a series of simulation studies. We begin by demonstrating our ability to recover branching process parameters

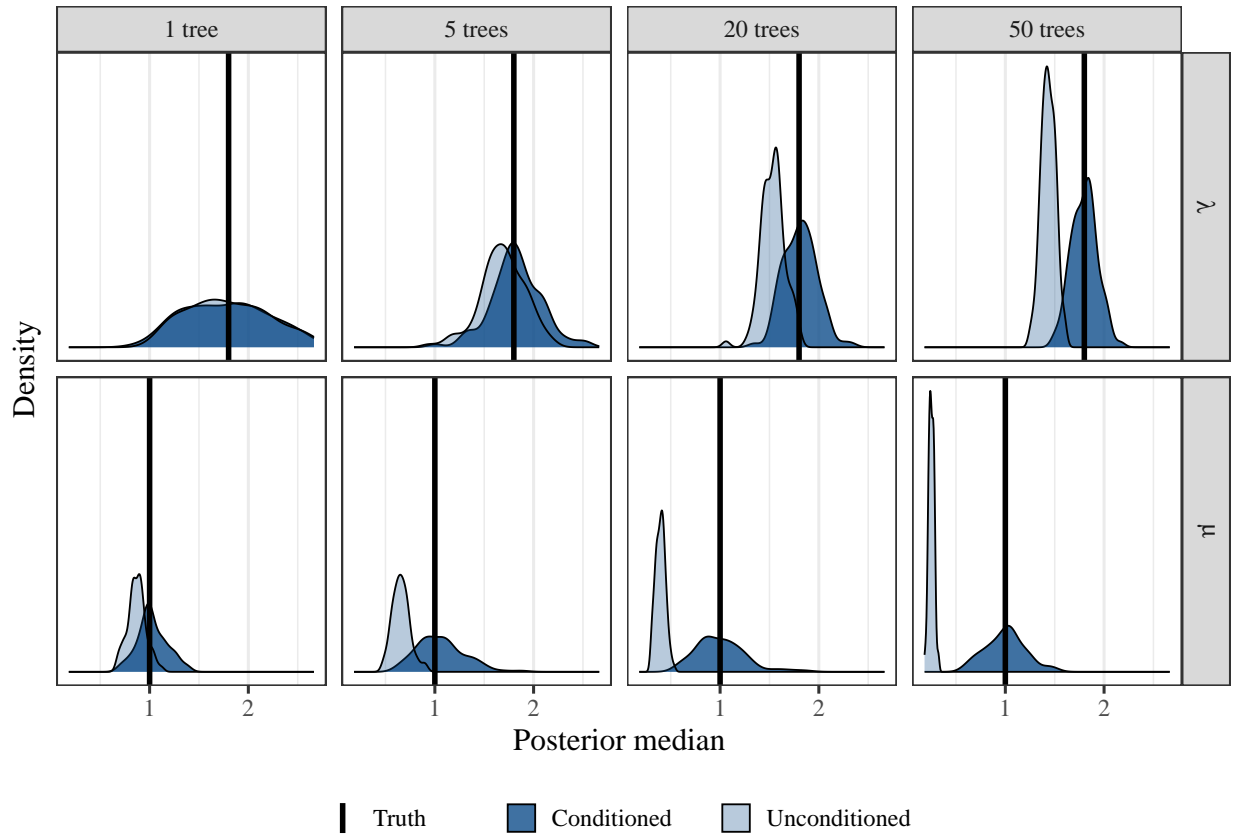


Figure 5: A simulation study demonstrating the importance of conditioning the tree model on the survival and observation of at least one lineage at collection time. Shown here are sampling distributions of posterior medians obtained from repeated runs of MCMC on different sets of trees. As larger tree sets are used for inference, the bias from using the unconditioned model becomes increasingly apparent, particularly for the death rate.

when trees are simulated directly from our process. We will then adjust the tree simulation setup to examine the effects of various model misspecifications on our inference. The ground truth setups for all simulation studies, chosen to reflect the data observed in experimentation and our prior knowledge (see Section *Analysis of experimental data*), are documented in Appendix *Additional simulation study details*. The prior distributions, chosen to enforce the sigmoidal function to be non-decreasing and non-negative, are documented in Appendix *Priors* and visualized in Fig 6(a).

The goal is to show that our parameters can be recovered from the following posterior:

$$p(\boldsymbol{\theta}|\mathbf{T}) \propto p(\boldsymbol{\theta}) \prod_i p_c(T_i|\boldsymbol{\theta}). \quad (7)$$

We generated 5 sets of 58 trees each, with each tree being the result of running the branching process for 15 units of time, to mimic our experimental setup. Trees that did not yield at least one surviving lineage to 15 units of time were discarded. The posterior distributions of birth rate and net birth rate curves (respectively, $\lambda(x)$ and $\lambda(x) - \mu$), compared to the truth, are shown for one tree set in Fig 6(b), “NM” column. Posterior histograms and traceplots of individual parameters, as well as the sigmoid posteriors for the remaining tree sets, are shown in Appendix *Additional simulation study details*. We see that the true birth rate sigmoid curve is contained within the 90% posterior credible band for birth rate curves.

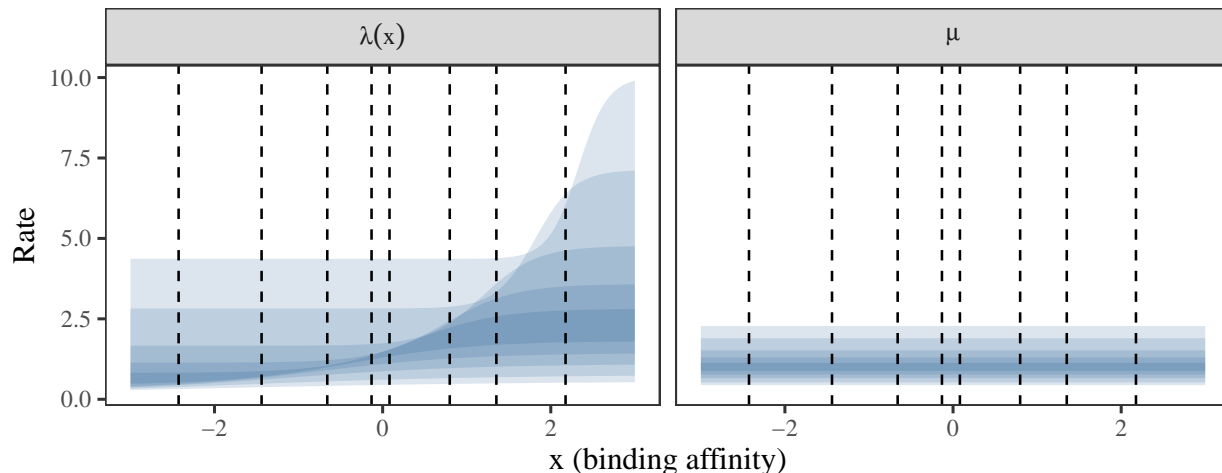
Birth rate recovery, approximation of the likelihood

As mentioned in Section *Related work*, Barido-Sottani et al. (2020) derive an approximate analytic solution to the multitype branching process, using an assumption that type changes do not occur in unsampled lineages. They motivate this approximation with analysis showing sufficiently good accuracy in their scientific context, paired with large computational performance gains compared to the numerical integration necessary to compute the correct likelihood. We implemented this method and determined that their assumption does not hold for our context. To see this, we run the simulation study in Section *Birth rate recovery, no model misspecification* again, but during inference, we use the approximate branching process likelihood instead of the correct likelihood (which requires numerical integration). The posterior distributions of sigmoid birth rate curves, compared to the truth, are shown for one tree set in Fig 6(b), “AL” column. Posterior histograms and traceplots of individual parameters, as well as the sigmoid posteriors for the remaining tree sets, are shown in Appendix *Additional simulation study details*. We see that the posterior over birth rate curves fails to capture the true curve at many points along the affinity (x) axis.

Birth rate recovery, incorrect sampling probability

To understand the robustness of our model to an incorrectly-known sampling probability ρ , we run the simulation study in Section *Birth rate recovery, no model misspecification* again, but during inference, we incorrectly set $\rho = 0.2$ instead of $\rho = 0.1$. The posterior distributions of sigmoid birth rate curves, compared to the truth, are shown for one tree set in Fig 6(b), “ISP” column. Posterior histograms and traceplots of individual parameters, as well as the sigmoid posteriors for the remaining tree sets, are shown in Appendix *Additional simulation study details*. We notice an underestimation bias of the birth rate curves, but note that the *net* birth rate curve is well-recovered.

(a) Priors



(b) Posteriors for each simulation study

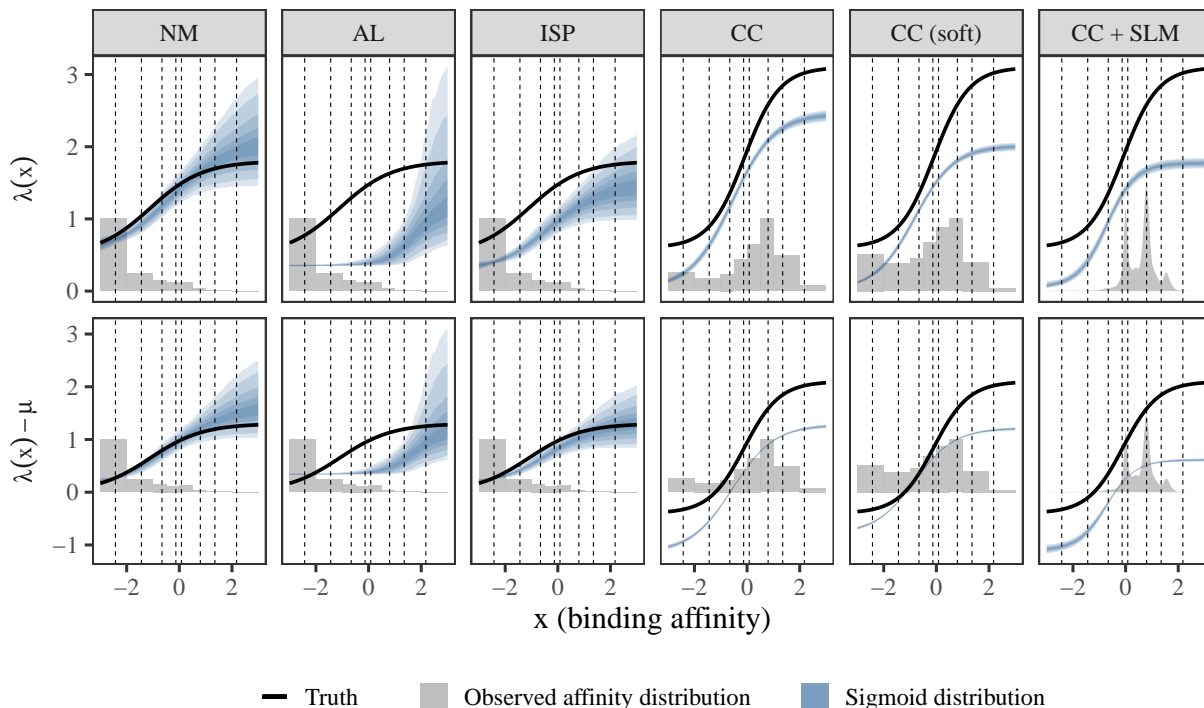


Figure 6: (a) The priors over the birth rate sigmoid and death rate scalar, used for all simulation studies and data analyses. Shaded regions represent credible intervals (the widest being 90%). The dashed lines show the values of the type space, i.e. the points at which the birth rate sigmoid is inferred. (b) The posteriors over the birth rate sigmoid for one run of each of four simulation studies, as well as the posteriors for the difference in birth rate and death rate, shown in blue. The abbreviations for the simulation study names are: NM, for no model misspecification; AL, for approximation of the likelihood; ISP, for incorrect sampling probability; CC, for carrying capacity; CC (soft), for soft carrying capacity; and CC+SLM, for carrying capacity with a sequence-level mutation process. The distributions of affinities observed in the simulated trees for each study are shown in gray.

Birth rate recovery, carrying capacity

Scientific consensus is that the germinal center has a carrying capacity for B cells. In the late stages of affinity maturation, the germinal center reaches a maximum cell population size and begins to inhibit the cells’ proliferation, potentially regardless of their antibodies’ binding affinity, to adjust evolutionary dynamics and control this population size. To understand the robustness of our model to experimental data sampled in such a phenomenon, we run the simulation study in Section *Birth rate recovery, no model misspecification* again, but with a carrying capacity implemented. When the number of living cells in the tree reaches 1000, a lineage is chosen uniformly randomly to die. The posterior distributions of sigmoid birth rate curves, compared to the truth, are shown for one tree set in Fig 6(b), “CC” column. Posterior histograms and traceplots of individual parameters, as well as the sigmoid posteriors for the remaining tree sets, are shown in Appendix *Additional simulation study details*. We notice an underestimation bias of both the birth rate and net birth rate curves; the branching process assumed for inference requires a lower overall birth rate to attempt to explain the observed distribution of tree sizes.

Note that the tighter posteriors in the carrying capacity studies can be attributed to the larger tree sizes used for inference in these studies. It is considerably easier to reliably simulate large trees in the presence of a capacity, which prevents tree size explosion.

Birth rate recovery, soft carrying capacity

To explore the effects of different implementations of a carrying capacity, we modified and repeated the simulation study in Section *Birth rate recovery, carrying capacity*. When the population reaches capacity in this study, rather than randomly selecting a lineage to die, we logistically modulate the birth rate such that the process is critical. The posterior distributions of sigmoid birth rate curves, compared to the truth, are shown for one tree set in Fig 6(b), “CC (soft)” column. Posterior histograms and traceplots of individual parameters, as well as the sigmoid posteriors for the remaining tree sets, are shown in Appendix *Additional simulation study details*. We notice a similar underestimation bias as in Section *Birth rate recovery, carrying capacity*, but with an additional effect of the range of the sigmoid being smaller compared to the sigmoid inferred under the hard carrying capacity model.

Birth rate recovery, carrying capacity with sequence-level mutation process

In the germinal center, B cell mutations occur on the sequence level; in our branching process, we assume type changes are Markovian with respect to the binding affinity, a function of the genetic sequence. Our model thus assumes an oversimplification of the B cell mutation process that needs to be examined. We run the simulation study in Section *Birth rate recovery, carrying capacity*, but the type space and type change rate matrix are replaced by the sequence-level mutation process described in Section *A priori estimation of type change rate matrix*. The posterior distributions of sigmoid birth rate curves, compared to the truth, are shown for one tree set in Fig 6(b), “CC+SLM” column. Posterior histograms and traceplots of individual parameters, as well as the sigmoid posteriors for the remaining tree sets, are shown in Appendix *Additional simulation study details*. We notice a similar underestimation bias and reduced sigmoid range as in Section *Birth rate recovery, soft carrying capacity*.

Analysis of experimental data

Data description

In experimentation, 18 genetically identical mice genetically unable to generate their own GCs received adoptive transfers of GC-competent monoclonal B cells specific for chIgY and were then immunized with this antigen to trigger GC formation. We observed the results of 52 parallel replications of affinity maturation—one for each germinal center sampled across the mice. B cells were sampled from the mice after 15 days, and the *Igh2.1* and *Igk2.1* alleles were sequenced with the Illumina MiSeq platform as described in DeWitt, Vora, Taraki et al. (2025) [9]. Sequences were aligned and concatenated, with the final 3,758 alignments having length 657 and no insertions or deletions.

As discussed in Section *Problem formulation*, we need to be able to estimate a phylogenetic tree with type annotations for each germinal center. To do so, we use the software package BEAST to sample 5,000 (after chain thinning) trees for each germinal center, from the posterior formed with the HKY substitution model and generalized Bayesian Skyline tree prior [37, 17, 11]. To obtain type change annotations, we use a feature implemented in BEAST for sampling ancestral states, as well as mutations which generate these ancestral states [29, 18]. Since we currently do not have the machinery to jointly infer rate parameters and phylogenies, we uniformly randomly select one tree from the resulting MCMC chain for each germinal center to use for inference.

Notably, we enforced each sampled tree to have the naive sequence at the root, since we controlled for this in experimentation. To do so, we introduced the naive sequence as a sampled leaf when configuring BEAST, setting the sampling time to a small positive $\epsilon \approx 0$. We then “inverted” the small ϵ -length branch in each sampled tree to have the naive sequence at the root. An example of one sampled tree from two different germinal centers is shown in Fig 2.

Parameter inference

We fix Γ and ρ_i as discussed in Section *Adapting our methodology to the experimental setup of DeWitt, Vora, Taraki et al. (2025)* and conduct inference of θ . Priors used are documented in Appendix *Priors*. The posterior distribution of sigmoid birth rate curves is shown in Fig 7. Posterior histograms and traceplots of individual parameters are shown in Appendix *Additional data analysis figures*.

We observe a sigmoid with a range roughly spanning the interval (0.1, 0.6), and with a steep transition near the zero-valued $-\Delta \log_{10} K_D$ region. In light of the observed effects of carrying capacity in our simulation studies, we suspect that these birth rate curves are underestimated. Nonetheless, the order of magnitude of the inferred birth rates corresponding to different BCR binding affinities is likely reasonable.

Recall from Section *Data description* that we use one tree sample per germinal center to conduct inference. This behavior ignores the phylogenetic uncertainty captured in the chain of tree samples from BEAST. To investigate the effect of ignoring this uncertainty, we ran additional analyses, using different tree samples for each germinal center. The results are also shown in Appendix *Additional data analysis figures*; we found the effect to be relatively minor. Some variation was observed in the posteriors for the birth rate curve, but the overall range of the curve remained consistent.

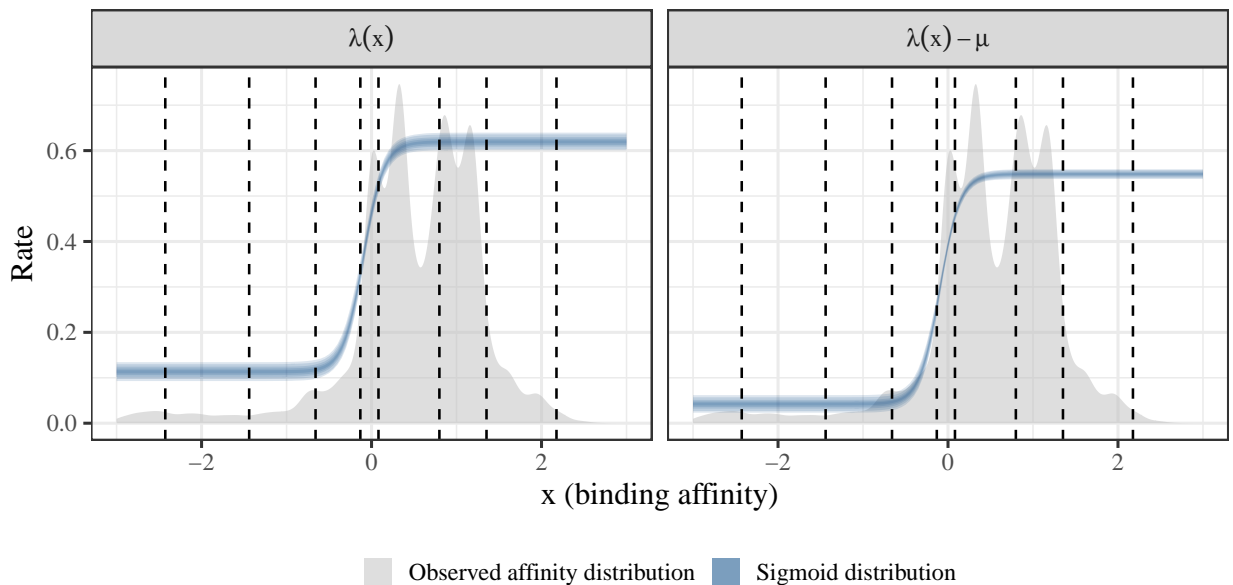


Figure 7: A comparison of the prior and posterior over sigmoid curves for the experimental data analysis, shown in blue. Shaded regions represent credible intervals (the widest being 90%). The dashed lines show the values of the type space, i.e. the points at which the birth rate sigmoid is inferred. The distribution of affinities observed in the BEAST trees is shown in gray.

Posterior predictive diagnostics

To examine how well our model fits the data, we perform posterior predictive diagnostics. Each posterior sample is used to generate a replicate set of germinal center data, by simulating 52 trees and collecting the sequences at the leaves. For each replicate, we produce 8 data summary statistics—the proportion of leaves with each of the 8 discretized binding affinity values, aggregated over all the trees. The distribution of each summary, compared to the observed proportion of each affinity value in the experimental data, is visualized in Appendix *Additional data analysis figures*. We note how the frequency of the fourth-largest affinity is overestimated, while those of the second and third-largest are underestimated. This indicates that the sigmoid inferred under our model may be too steep. We suspect this could be a consequence of not modeling the germinal’s carrying capacity.

Discussion

In this paper, we developed a multitype branching process with the flexibility to model a functional relationship between birth rates and lineage attributes. We then applied this model to a novel experiment studying antibody affinity maturation to illuminate how antibody binding affinity translates into B cell fitness in the germinal center. We reiterate that this relationship cannot be measured directly and poses a long-standing problem in the field of immunology [22, 4].

In simulation studies, we found that a sigmoidal mapping of affinity to B cell birth rate could be recovered if the data-generating process is indeed our branching process, but showed the biases that can occur under a more biologically-accurate data-generating process with a carrying capacity. We also found that the presence of replicate evolutionary processes

contributes to an underestimation bias of the birth and death rates if one does not condition on non-extinction. Finally, we observed that the approximate likelihood of Barido-Sottani et al. (2020) did not perform well in our context. This may be a result of the large number of lineages that go unobserved, whether due to the B cells being eliminated or merely going unsampled.

In data analysis, we inferred a sigmoidal mapping that indicates a factor of 6 difference in birth rate for high-affinity vs low-affinity B cells. Seeing how the carrying capacity simulation studies indicate a potential bias of vertical compression for the sigmoid curve, we conjecture that the true difference is even larger than a factor of 6. While this analysis has limitations, which we address below, to our knowledge this is the first phylogenetic-based attempt to infer the affinity-fitness relationship in the germinal center from BCR sequence data.

There are a few limitations of our method that, if overcome, could provide for a more biologically faithful analysis of this germinal center data. First, we are not jointly inferring the birth rate mapping with the phylogenetic trees, and use only one tree per germinal center for a given analysis. This could underestimate uncertainty around our branching process parameters (also see Appendix *Additional data analysis figures*). We could conduct joint inference by building a hierarchical model, where our branching process density serves as the prior over the phylogenetic tree. In this manner, both the tree and birth rate mapping are inferred directly from the observed genetic sequences. The implementation of such a hierarchical model can be computationally challenging, though, as the MCMC algorithm would need to operate over a state space involving trees. A potential alternative to this solution could be a sampling importance resampling procedure with our existing tree samples, although this would require that the prior density which generated our samples is sufficiently similar to our branching process density [16, 23].

Second, as discussed in Section *Birth rate recovery, carrying capacity* and Section *Posterior predictive diagnostics*, there is a consequential model misspecification when not accounting for the carrying capacity of the germinal center. DeWitt, Vora, Taraki et al. (2025) used a non-phylogenetic traveling wave model that accounts for carrying capacity to infer the affinity-fitness relationship [9]. However, this model was fit to bulk, not single-cell, data collected at multiple time points. The work of Ralph et al. (2025) provides a framework more comparable to ours [31]. These authors use deep learning and simulation-based inference to obtain the affinity-fitness relationship under a branching process model with a carrying capacity constraint, enforced by a birth rate modulated by the number of germinal center cells. This is the same model we use in our simulation study described in Section *Birth rate recovery, soft carrying capacity*. Ralph et al. (2025) discuss similarities and differences between our birth rate and their effective/modulated birth rate in their Discussion section. In short, the main difference is that our sigmoidal inference shows a sharp increase in birth rate as the BCR binding affinity increases, while Ralph et al. (2025) infer a more gradual increase in effective birth rate. They suggest that our sharp increase could be a result of not modeling carrying capacity, which is plausible.

One experimental way our branching process framework could avoid the effects of this misspecification is by collecting B cell sequence data at an earlier point in time during the affinity maturation process, before the germinal center achieves its capacity. A more model-based solution, though, could be to allow for time-varying rate parameters in the branching process. Stadler (2011) describes a branching process in which the birth and death rates are piecewise-constant over a set of time intervals [33]. Magee et al. (2020) brings this work into a Bayesian context, exploring both Gaussian and horseshoe Markov random field priors for the rates [26]. One could lower the y-scale parameter (ϕ_1) of the birth rate sigmoid in this

manner, at a time at which carrying capacity has kicked in. Alternatively, recent work by DeWitt et al. (2024) discuss how the branching process with a carrying capacity can have a tractable likelihood if a mean-field approach to modeling lineage interactions is taken [8].

Finally, future work could improve the manner in which we specify the affinity-fitness relationship. In this work, we specifically assumed a parametric sigmoidal form for the birth rate function. This form may not hold in practice. Instead, a Bayesian non-parametric approach could provide the flexibility necessary to avoid potential misspecification of the function; Gaussian processes or adaptive spline methods could prove useful for this task. Moreover, to relax the assumption that the same functional form governs the affinity-fitness relationship across mice, or even across individual germinal centers, Bayesian hierarchical techniques could be used to capture this potential heterogeneity.

Acknowledgments

This material is based upon work supported by the National Science Foundation Graduate Research Fellowship Program under Grant No DGE-1839285. Any opinions, findings, and conclusions or recommendations expressed in this material are those of the authors and do not necessarily reflect the views of the National Science Foundation.

References

- [1] Rhys M Adams, Thierry Mora, Aleksandra M Walczak, and Justin B Kinney. Measuring the sequence-affinity landscape of antibodies with massively parallel titration curves. *Elife*, 5:e23156, 2016.
- [2] Joëlle Barido-Sottani, Timothy G Vaughan, and Tanja Stadler. A multitype birth-death model for Bayesian inference of lineage-specific birth and death rates. *Systematic Biology*, 69(5):973–986, 2020.
- [3] Facundo D Batista and Michael S Neuberger. Affinity dependence of the b cell response to antigen: A threshold, a ceiling, and the importance of off-rate. *Immunity*, 8(6):751–759, 1998.
- [4] Facundo D Batista and Michael S Neuberger. Affinity dependence of the b cell response to antigen: A threshold, a ceiling, and the importance of off-rate. *Immunity*, 8(6):751–759, 1998.
- [5] Jeremy M Beaulieu and Brian C O’Meara. Detecting hidden diversification shifts in models of trait-dependent speciation and extinction. *Systematic Biology*, 65(4):583–601, 2016.
- [6] Jeff Bezanson, Alan Edelman, Stefan Karpinski, and Viral B Shah. Julia: A fresh approach to numerical computing. *SIAM review*, 59(1):65–98, 2017.
- [7] Ang Cui, Roberto Di Niro, Jason A Vander Heiden, Adrian W Briggs, Kris Adams, Tamara Gilbert, Kevin C O’Connor, Francois Vigneault, Mark J Shlomchik, and Steven H Kleinstein. A model of somatic hypermutation targeting in mice based on high-throughput Ig sequencing data. *The Journal of Immunology*, 197(9):3566–3574, 2016.

- [8] William S. DeWitt, Steven N. Evans, Ella Hiesmayr, and Sebastian Hummel. Mean-field interacting multi-type birth-death processes with a view to applications in phylodynamics, 2024.
- [9] William S DeWitt, Ashni A Vora, Tatsuya Araki, Jared G Galloway, Tanwee Alkutkar, Juliana Bortolatto, Tiago BR Castro, Will Dumm, Chris Jennings-Schaffer, Tongqiu Jia, et al. Replaying germinal center evolution on a quantified affinity landscape. *bioRxiv*, pages 2025–06, 2025.
- [10] Alexei J Drummond, Oliver G Pybus, Andrew Rambaut, Roald Forsberg, and Allen G Rodrigo. Measurably evolving populations. *Trends in Ecology & Evolution*, 18(9):481–488, 2003.
- [11] Alexei J Drummond, Andrew Rambaut, BETH Shapiro, and Oliver G Pybus. Bayesian coalescent inference of past population dynamics from molecular sequences. *Molecular Biology and Evolution*, 22(5):1185–1192, 2005.
- [12] Sebastian Duchene, Philippe Lemey, Tanja Stadler, Simon YW Ho, David A Duchene, Vijaykrishna Dhanasekaran, and Guy Baele. Bayesian evaluation of temporal signal in measurably evolving populations. *Molecular Biology and Evolution*, 37(11):3363–3379, 2020.
- [13] Richard G FitzJohn. Quantitative traits and diversification. *Systematic Biology*, 59(6):619–633, 2010.
- [14] Richard G FitzJohn. Diversitree: comparative phylogenetic analyses of diversification in R. *Methods in Ecology and Evolution*, 3(6):1084–1092, 2012.
- [15] Hong Ge, Kai Xu, and Zoubin Ghahramani. Turing: a language for flexible probabilistic inference. In *International Conference on Artificial Intelligence and Statistics, AISTATS 2018, 9-11 April 2018, Playa Blanca, Lanzarote, Canary Islands, Spain*, pages 1682–1690, 2018.
- [16] Neil J Gordon, David J Salmond, and Adrian FM Smith. Novel approach to nonlinear/non-Gaussian Bayesian state estimation. *IEE Proceedings F (Radar and Signal Processing)*, 140(2):107–113, 1993.
- [17] Masami Hasegawa, Hirohisa Kishino, and Taka-aki Yano. Dating of the human-ape splitting by a molecular clock of mitochondrial dna. *Journal of Molecular Evolution*, 22:160–174, 1985.
- [18] Asger Hobolth and Eric A Stone. Simulation from endpoint-conditioned, continuous-time Markov chains on a finite state space, with applications to molecular evolution. *The Annals of Applied Statistics*, 3(3):1204, 2009.
- [19] Matthew D Hoffman, Andrew Gelman, et al. The no-u-turn sampler: adaptively setting path lengths in hamiltonian monte carlo. *Journal of Machine Learning Research*, 15(1):1593–1623, 2014.
- [20] Steven H. Kleinstein, Yoram Louzoun, and Mark J. Shlomchik. Estimating hypermutation rates from clonal tree data 1. *The Journal of Immunology*, 171(9):4639–4649, 11 2003.

- [21] Denise Kühnert, Tanja Stadler, Timothy G Vaughan, and Alexei J Drummond. Phylogenetics with migration: a computational framework to quantify population structure from genomic data. *Molecular biology and evolution*, 33(8):2102–2116, 2016.
- [22] Masayuki Kuraoka, Aaron G. Schmidt, Takuya Nojima, Feng Feng, Akiko Watanabe, Daisuke Kitamura, Stephen C. Harrison, Thomas B. Kepler, and Garnett Kelsoe. Complex antigens drive permissive clonal selection in germinal centers. *Immunity*, 44(3):542–552, 2016.
- [23] Li-Jung Liang and Robert E Weiss. A hierarchical semiparametric regression model for combining hiv-1 phylogenetic analyses using iterative reweighting algorithms. *Biometrics*, 63(3):733–741, 2007.
- [24] Ailene MacPherson, Stilianos Louca, Angela McLaughlin, Jeffrey B Joy, and Matthew W Pennell. Unifying phylogenetic birth–death models in epidemiology and macroevolution. *Systematic Biology*, 71(1):172–189, 2022.
- [25] Wayne P Maddison, Peter E Midford, and Sarah P Otto. Estimating a binary character’s effect on speciation and extinction. *Systematic biology*, 56(5):701–710, 2007.
- [26] Andrew F Magee, Sebastian Höhna, Tetyana I Vasylyeva, Adam D Leaché, and Vladimir N Minin. Locally adaptive Bayesian birth-death model successfully detects slow and rapid rate shifts. *PLoS Computational Biology*, 16(10):e1007999, 2020.
- [27] Christian T. Mayer, Anna Gazumyan, Ervin E. Kara, Alexander D. Gitlin, Jovana Golijanin, Charlotte Viant, Joy Pai, Thiago Y. Oliveira, Qiao Wang, Amelia Escolano, Max Medina-Ramirez, Rogier W. Sanders, and Michel C. Nussenzweig. The microanatomic segregation of selection by apoptosis in the germinal center. *Science*, 358(6360):eaao2602, 2017.
- [28] Sean Nee, Robert Mcredie May, and Paul H Harvey. The reconstructed evolutionary process. *Philosophical Transactions of the Royal Society of London. Series B: Biological Sciences*, 344(1309):305–311, 1994.
- [29] Rasmus Nielsen. Mapping mutations on phylogenies. *Systematic Biology*, 51(5):729–739, 2002.
- [30] Christopher Rackauckas and Qing Nie. DifferentialEquations.jl—a performant and feature-rich ecosystem for solving differential equations in Julia. *Journal of Open Research Software*, 5(1), 2017.
- [31] Duncan K Ralph, Athanasios G Bakis, Jared Galloway, Ashni Vora, Tatsuya Araki, Gabriel D Victora, Yun S Song, William S DeWitt III, and Frederick A Matsen IV. Inference of germinal center affinity-fitness response functions via deep learning. *In preparation*, 2025.
- [32] Aylwyn Scally and Richard Durbin. Revising the human mutation rate: implications for understanding human evolution. *Nature Reviews Genetics*, 13(10):745–753, 2012.
- [33] Tanja Stadler. Mammalian phylogeny reveals recent diversification rate shifts. *Proceedings of the National Academy of Sciences*, 108(15):6187–6192, 2011.

- [34] Tanja Stadler. How can we improve accuracy of macroevolutionary rate estimates? *Systematic Biology*, 62(2):321–329, 2013.
- [35] Tanja Stadler. Recovering speciation and extinction dynamics based on phylogenies. *Journal of Evolutionary Biology*, 26(6):1203–1219, 2013.
- [36] Tanja Stadler and Sebastian Bonhoeffer. Uncovering epidemiological dynamics in heterogeneous host populations using phylogenetic methods. *Philosophical Transactions of the Royal Society B: Biological Sciences*, 368(1614):20120198, 2013.
- [37] Marc A Suchard, Philippe Lemey, Guy Baele, Daniel L Ayres, Alexei J Drummond, and Andrew Rambaut. Bayesian phylogenetic and phylodynamic data integration using BEAST 1.10. *Virus Evolution*, 4(1):vey016, 06 2018.
- [38] Gabriel D Victora and Michel C Nussenzweig. Germinal centers. *Annual review of immunology*, 40(1):413–442, 2022.
- [39] Christopher Vollmers, Rene V Sit, Joshua A Weinstein, Cornelia L Dekker, and Stephen R Quake. Genetic measurement of memory B-cell recall using antibody repertoire sequencing. *Proceedings of the National Academy of Sciences*, 110(33):13463–13468, 2013.
- [40] Gur Yaari, Jason A Vander Heiden, Mohamed Uduman, Daniel Gadala-Maria, Namita Gupta, Joel NH Stern, Kevin C O’Connor, David A Hafler, Uri Laserson, Francois Vigneault, et al. Models of somatic hypermutation targeting and substitution based on synonymous mutations from high-throughput immunoglobulin sequencing data. *Frontiers in Immunology*, 4:358, 2013.

Supplementary Materials

Additional simulation study details

No model misspecification

The following parameter values and figures correspond to the simulation study described in Section *Birth rate recovery, no model misspecification*. The parameter values configure the data generating process used to simulate each tree for the 5 tree sets used in the study. The first figure demonstrates the performance of our method by visualizing the posterior over sigmoid curves inferred for each tree set. The second figure decomposes this posterior visualization into posterior histograms for each sigmoid parameter individually, as well as for the other branching process parameters. Finally, the third figure shows traceplots for each of these parameters. The subsequent sections of this appendix for each other simulation study are structured in the same manner.

Ground truth parameter values

- $\phi = [1.3, 1, -1.1, 0.5]$
- $\mu = 0.5$
- $\delta = 20$
- $\rho = 0.1$

The type space and type change rate matrix are taken from Sections *Discretization of affinity values for type space* and *A priori estimation of type change rate matrix*, respectively.

Additional figures

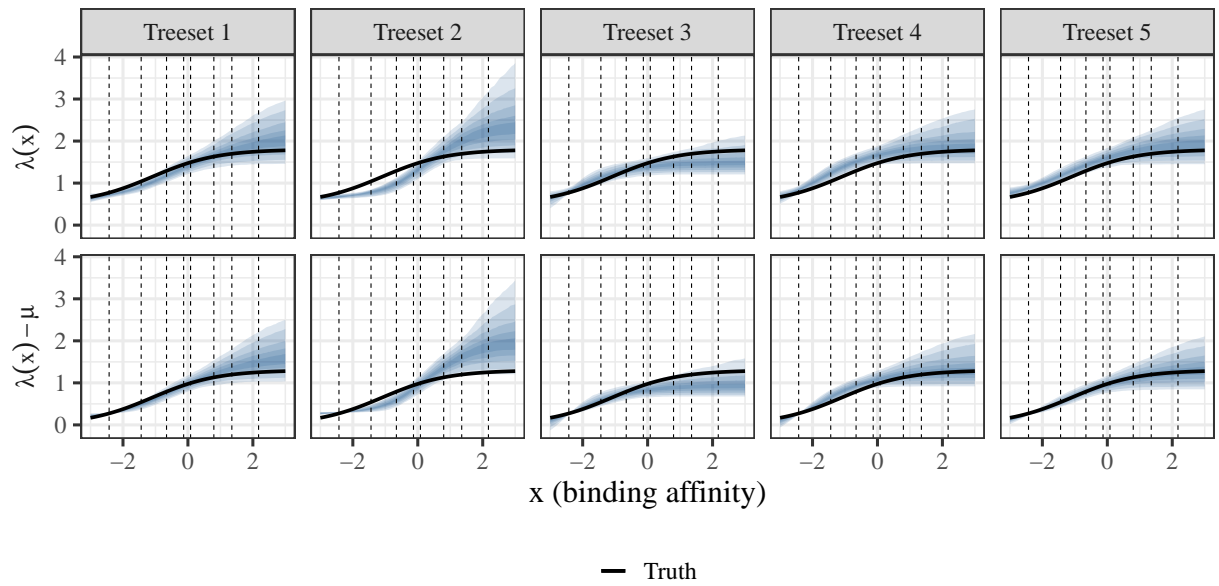


Figure 8: (**No model misspecification**) Posteriors of the birth rate sigmoid and difference in birth rate and death rate, for each tree set. Shaded regions represent credible intervals (the widest being 90%). The dashed lines show the values of the type space, i.e. the points at which the birth rate sigmoid is inferred.

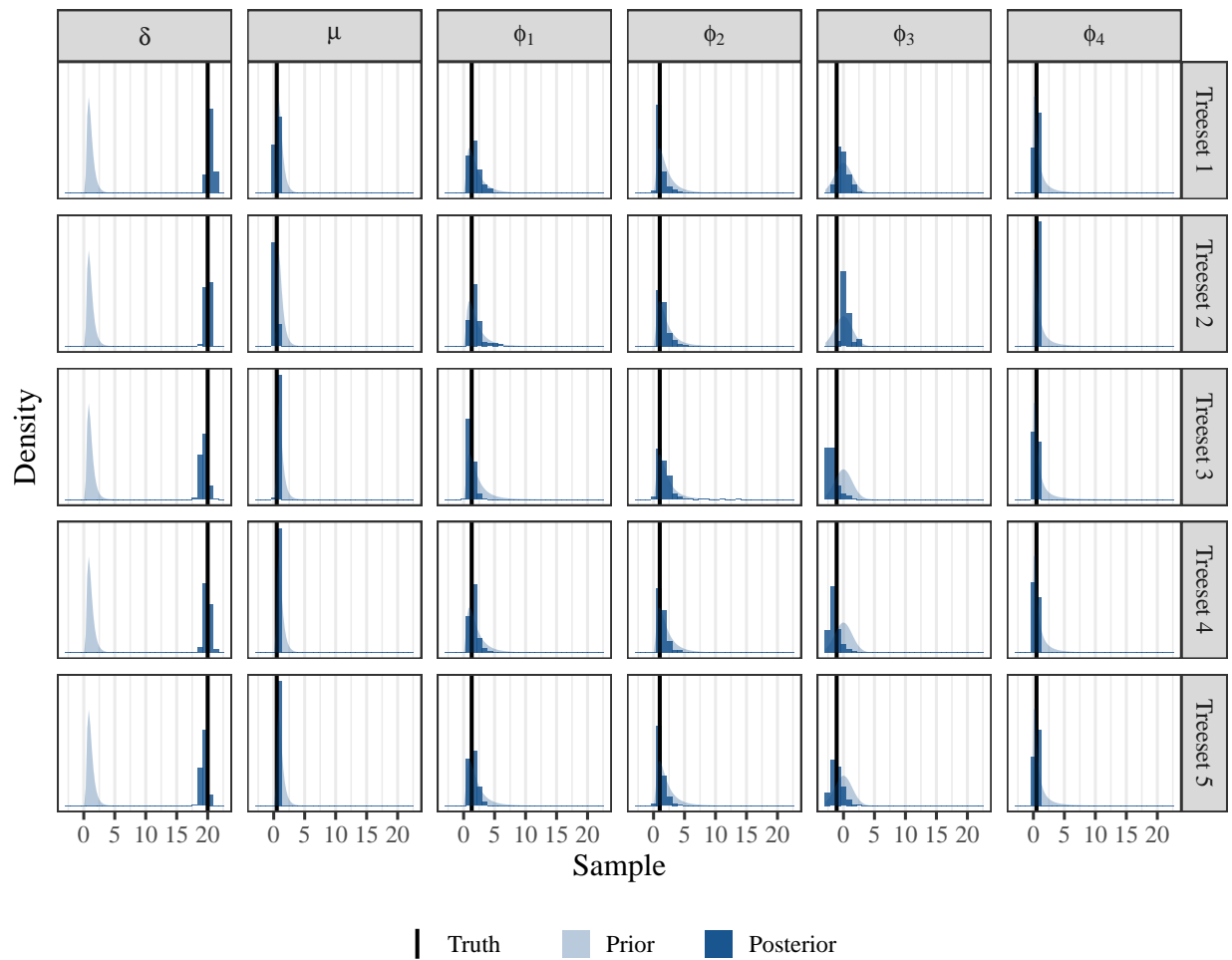


Figure 9: **(No model misspecification)** Posterior histograms and prior density curves of each parameter, for each tree set.

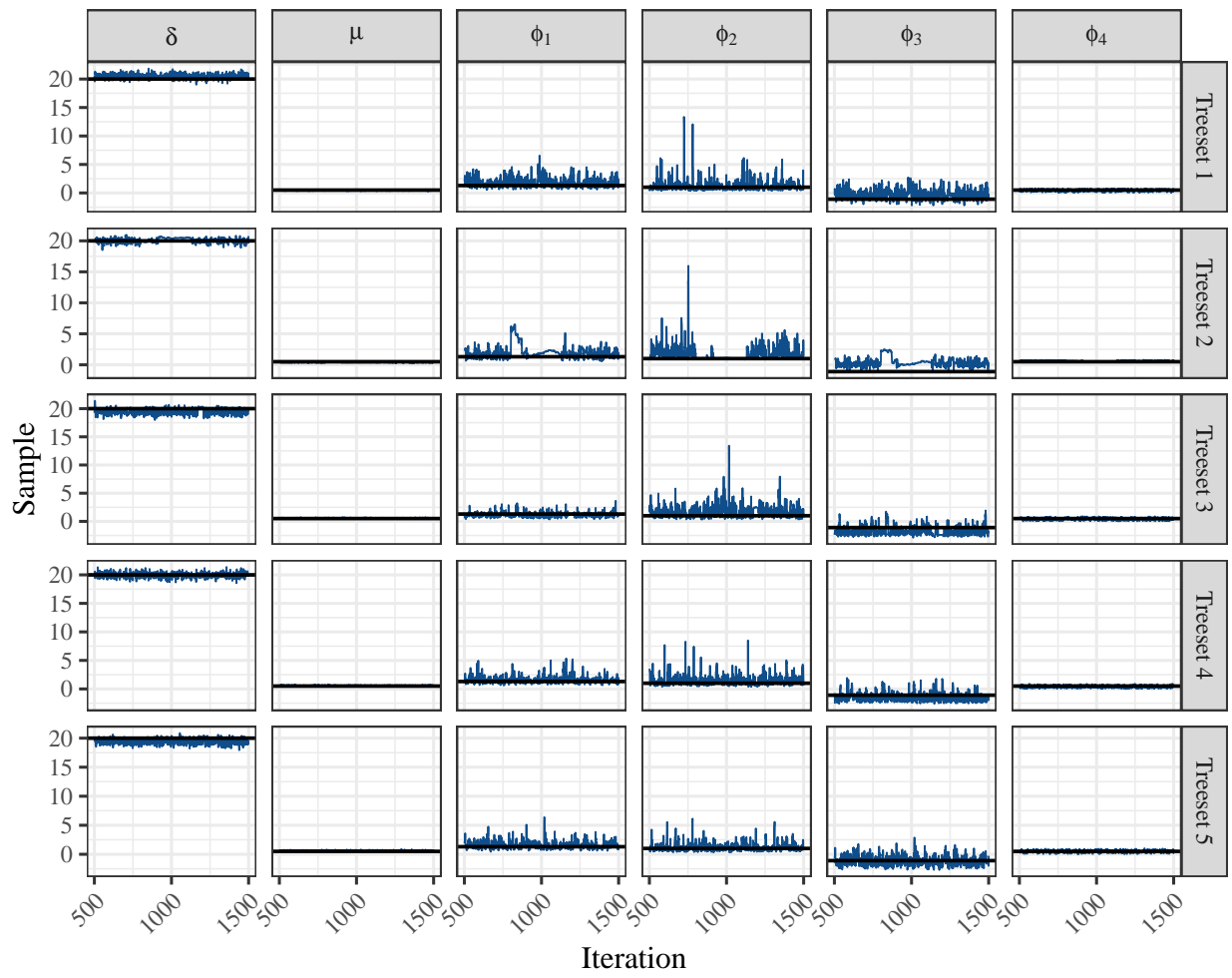


Figure 10: (No model misspecification) Posterior traceplots of each parameter, for each tree set.

Approximation of the likelihood

The following parameter values and figures correspond to the simulation study described in Section *Birth rate recovery, approximation of the likelihood*.

Ground truth parameter values

- $\phi = [1.3, 1, -1.1, 0.5]$
- $\mu = 0.5$
- $\delta = 20$
- $\rho = 0.1$

The type space and type change rate matrix are taken from Sections *Discretization of affinity values for type space* and *A priori estimation of type change rate matrix*, respectively.

Additional figures

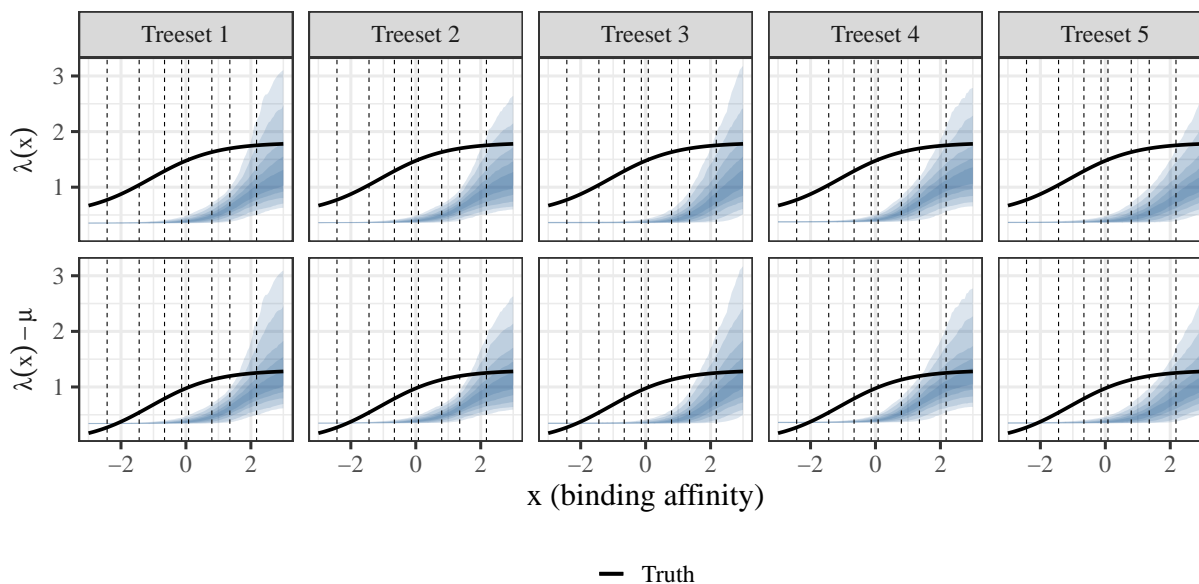


Figure 11: **(Approximation of the likelihood)** Posteriors of the birth rate sigmoid and difference in birth rate and death rate, for each tree set. Shaded regions represent credible intervals (the widest being 90%). The dashed lines show the values of the type space, i.e. the points at which the birth rate sigmoid is inferred.

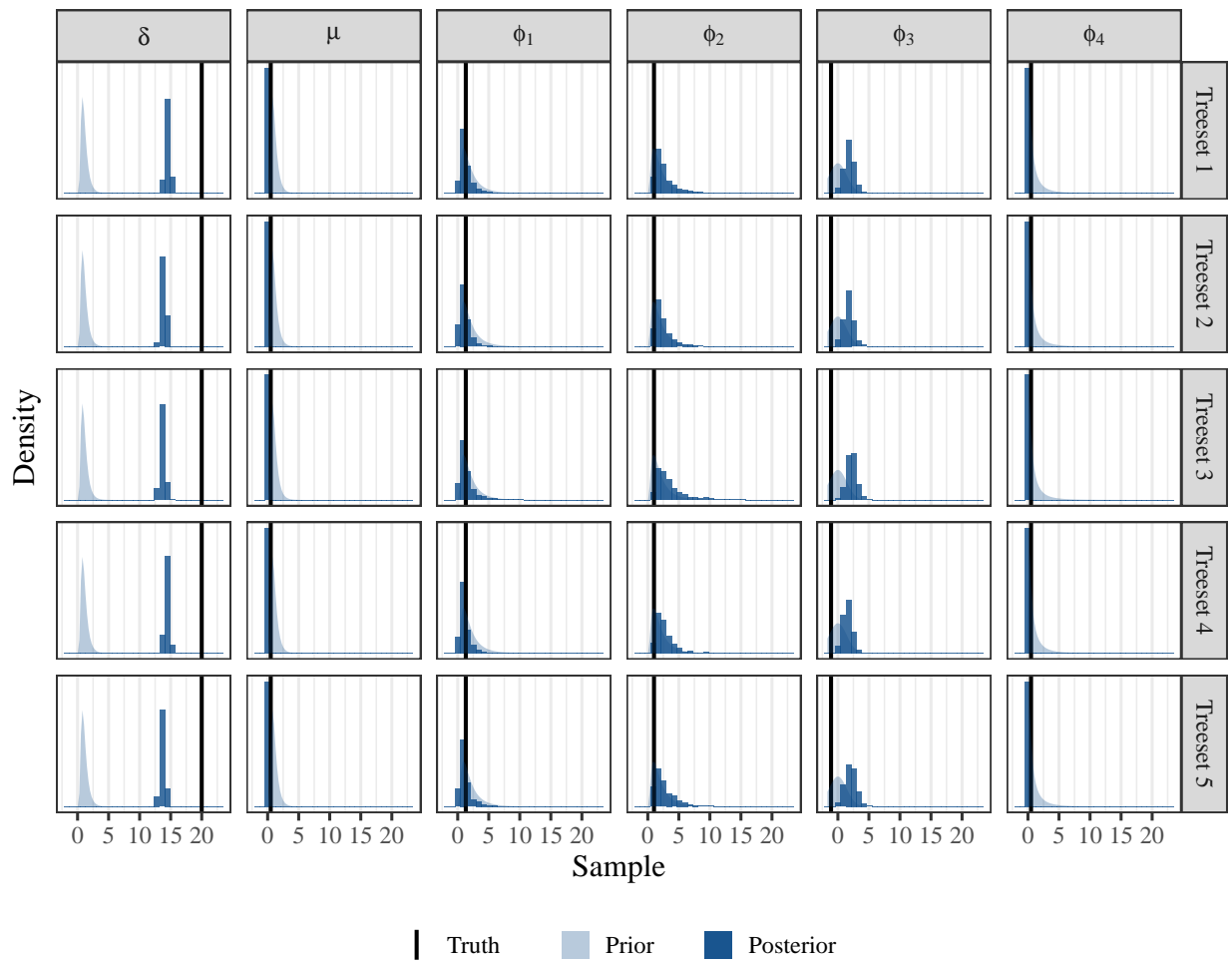


Figure 12: **(Approximation of the likelihood)** Posterior histograms and prior density curves of each parameter, for each tree set.

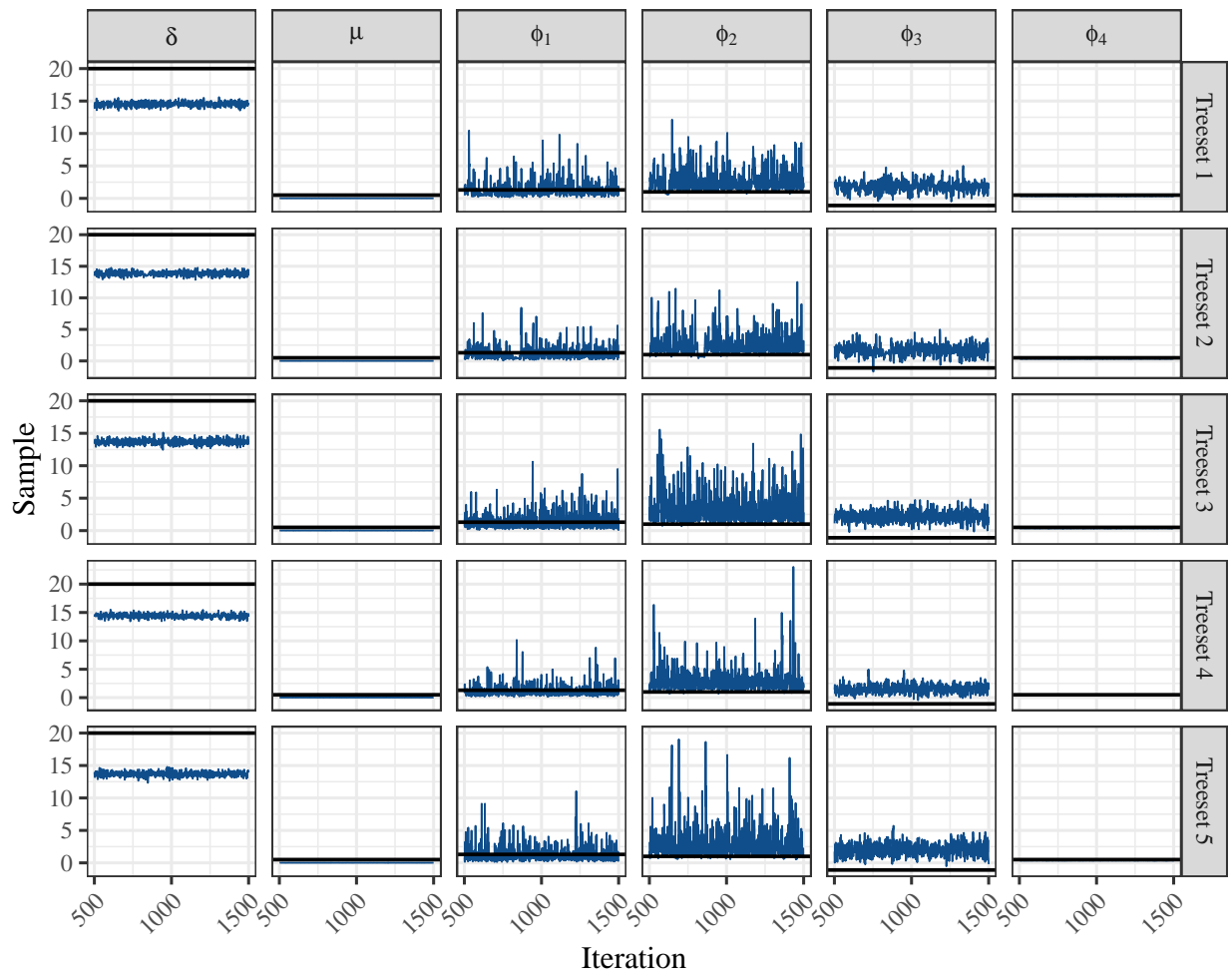


Figure 13: **(Approximation of the likelihood)** Posterior traceplots of each parameter, for each tree set.

Incorrect sampling probability

The following parameter values and figures correspond to the simulation study described in Section *Birth rate recovery, incorrect sampling probability*.

Ground truth parameter values

- $\phi = [1.3, 1, -1.1, 0.5]$
- $\mu = 0.5$
- $\delta = 20$
- $\rho = 0.1$

The type space and type change rate matrix are taken from Sections *Discretization of affinity values for type space* and *A priori estimation of type change rate matrix*, respectively.

During inference, ρ is set to be 0.2.

Additional figures

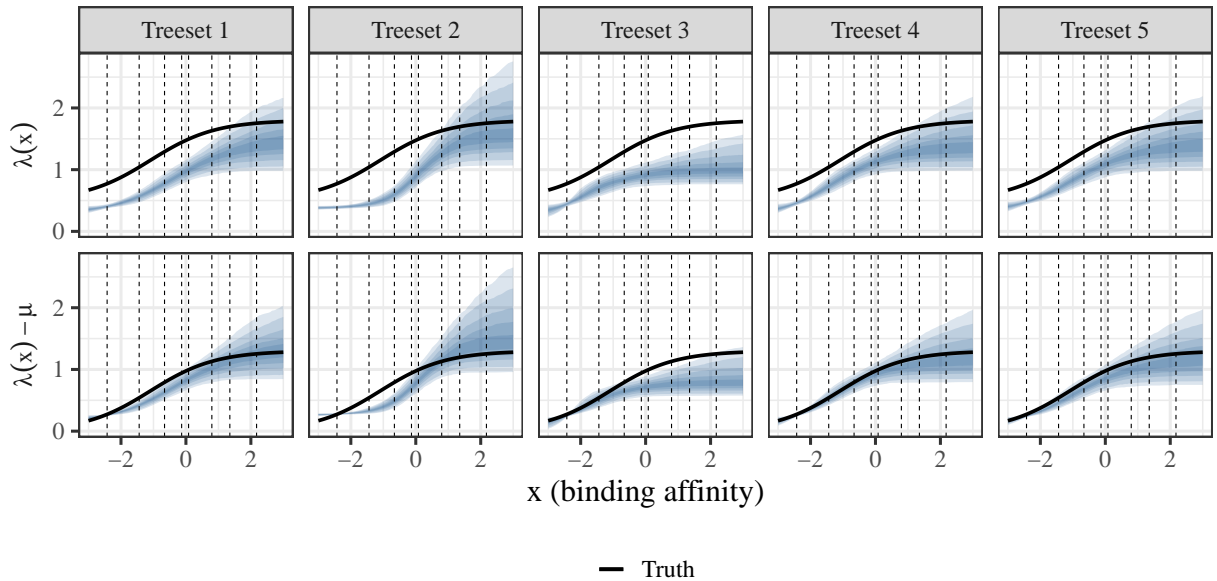


Figure 14: (**Incorrect sampling probability**) Posteriors of the birth rate sigmoid and difference in birth rate and death rate, for each tree set. Shaded regions represent credible intervals (the widest being 90%). The dashed lines show the values of the type space, i.e. the points at which the birth rate sigmoid is inferred.

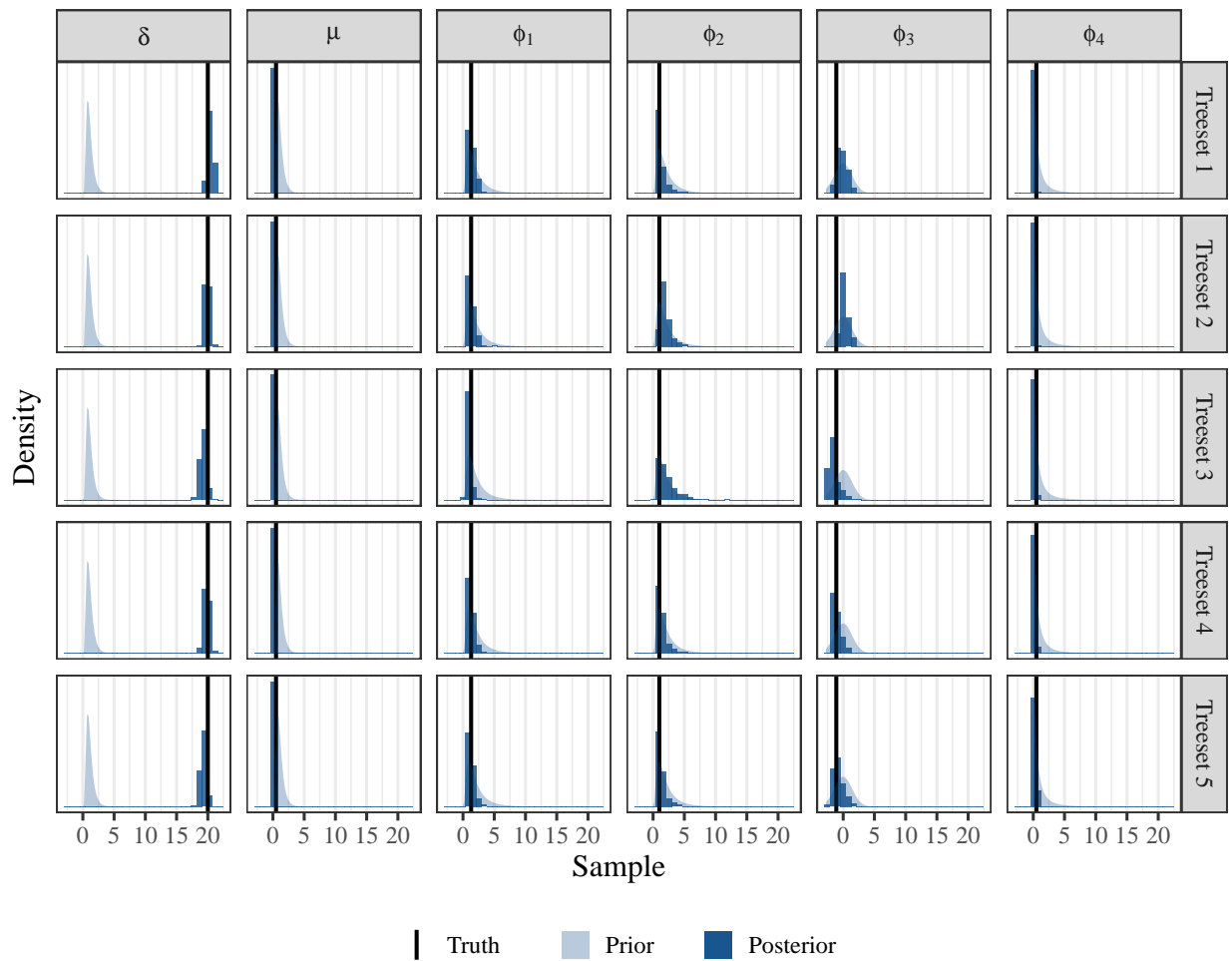


Figure 15: **(Incorrect sampling probability)** Posterior histograms and prior density curves of each parameter, for each tree set.

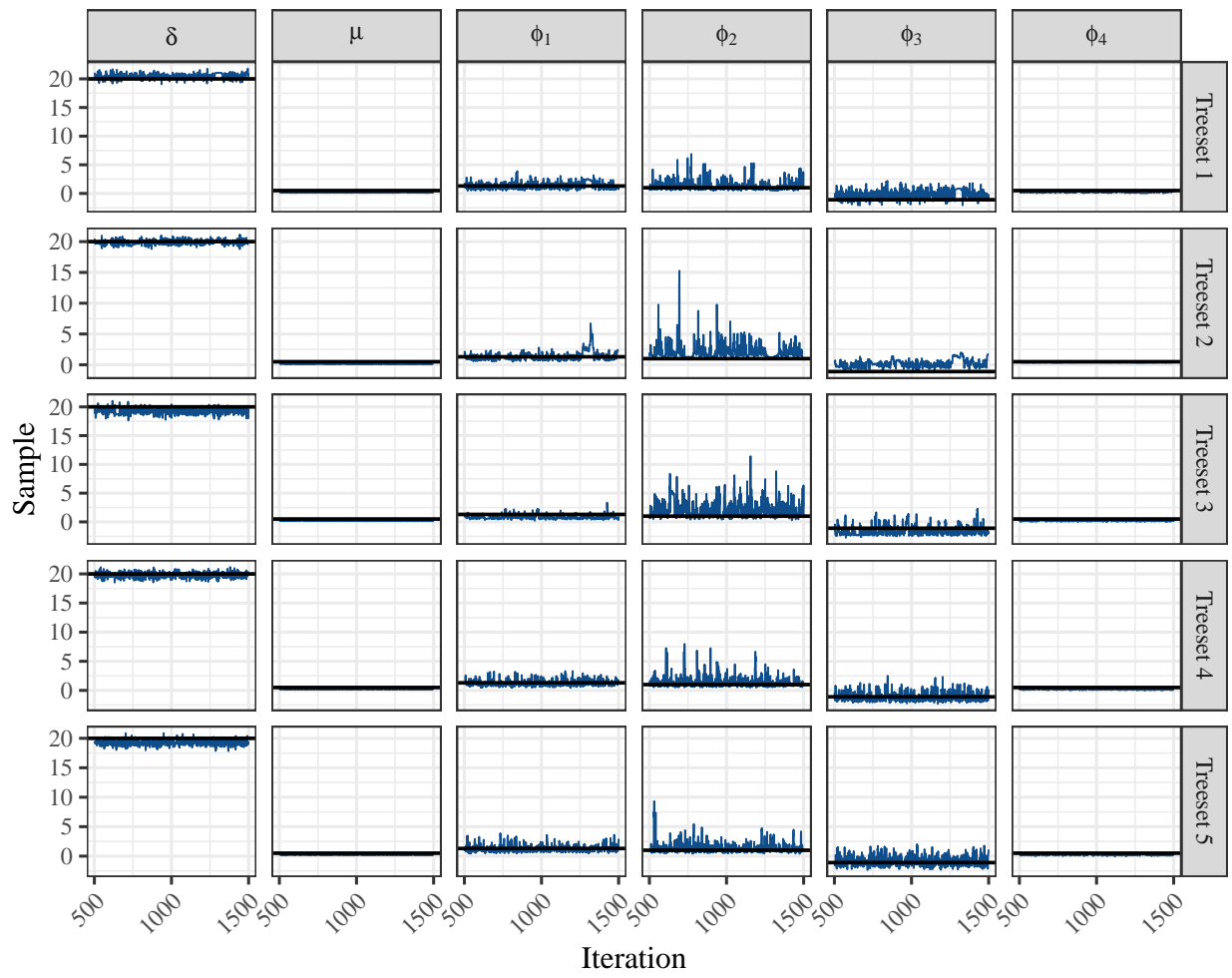


Figure 16: **(Incorrect sampling probability)** Posterior traceplots of each parameter, for each tree set.

Carrying capacity

The following parameter values and figures correspond to the simulation study described in Section *Birth rate recovery, carrying capacity*.

Ground truth parameter values

- $\phi = [2.5, 1.5, -0.1, 0.6]$
- $\mu = 1$
- $\delta = 1$
- $\rho = 0.1$

The type space and type change rate matrix are taken from Sections *Discretization of affinity values for type space* and *A priori estimation of type change rate matrix*, respectively.

The carrying capacity is set to be 1000.

Additional figures

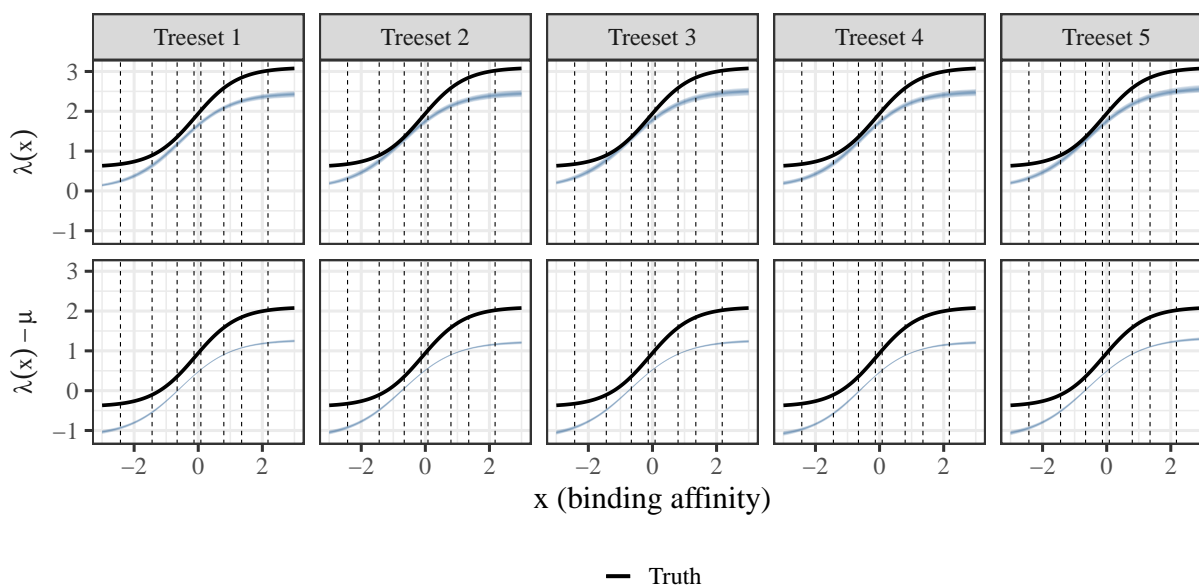


Figure 17: (**Carrying capacity**) Posteriors of the birth rate sigmoid and difference in birth rate and death rate, for each tree set. Shaded regions represent credible intervals (the widest being 90%). The dashed lines show the values of the type space, i.e. the points at which the birth rate sigmoid is inferred.

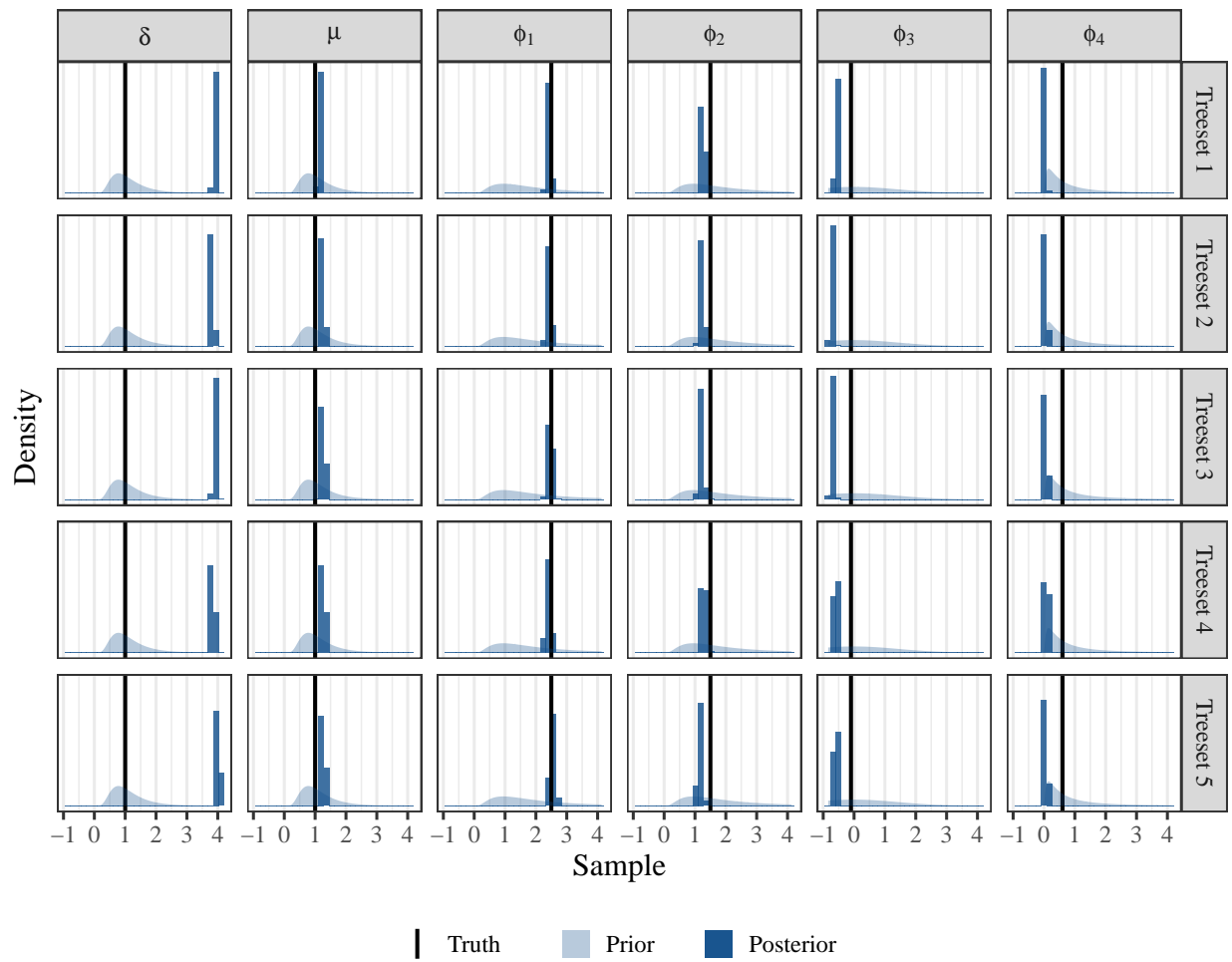


Figure 18: **(Carrying capacity)** Posterior histograms and prior density curves of each parameter, for each tree set.

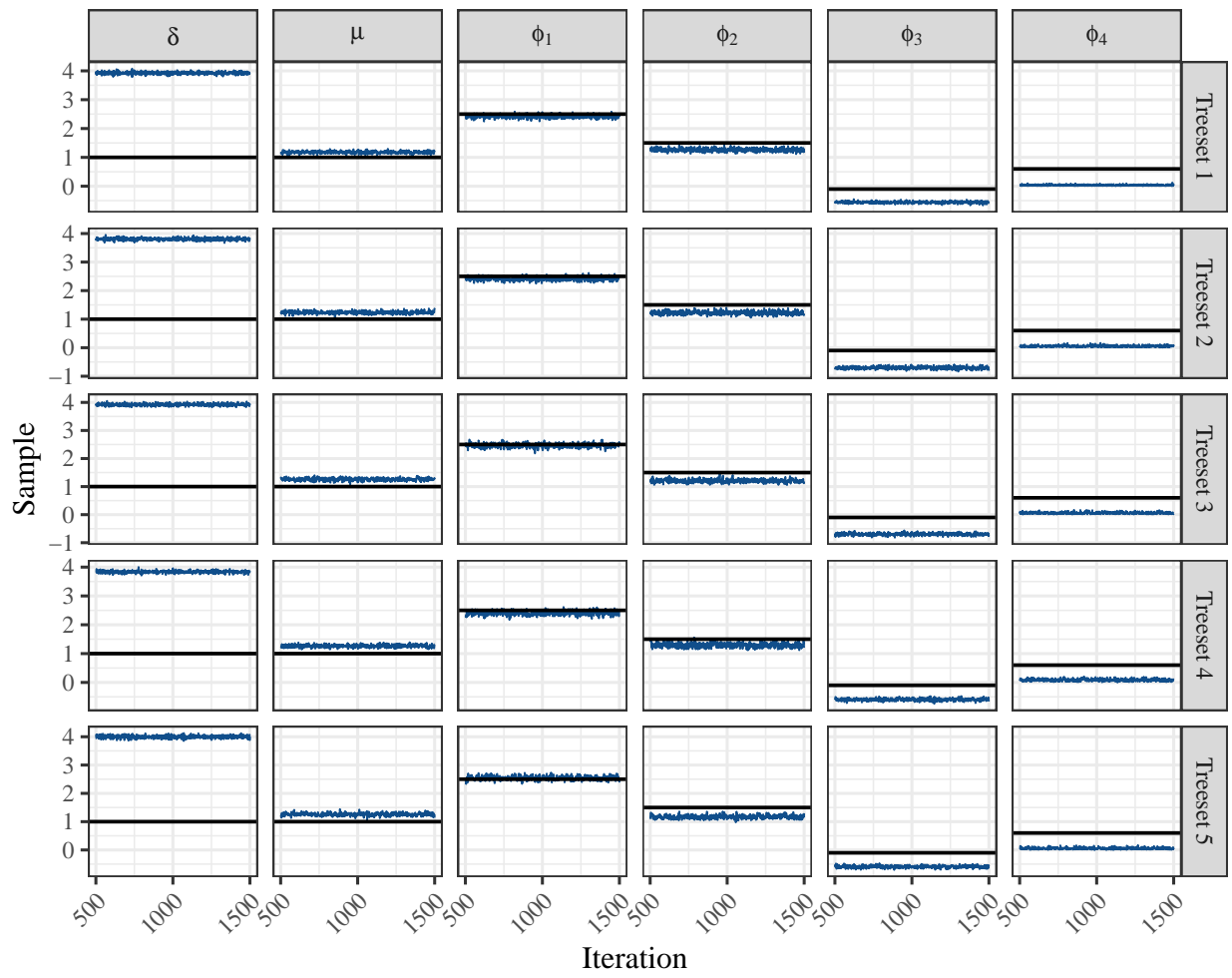


Figure 19: (Carrying capacity) Posterior traceplots of each parameter, for each tree set.

Soft carrying capacity

The following parameter values and figures correspond to the simulation study described in Section *Birth rate recovery, soft carrying capacity*.

Ground truth parameter values

- $\phi = [2.5, 1.5, -0.1, 0.6]$
- $\mu = 1$
- $\delta = 1$
- $\rho = 0.1$

The type space and type change rate matrix are taken from Sections *Discretization of affinity values for type space* and *A priori estimation of type change rate matrix*, respectively.

The carrying capacity is set to be 1000.

Additional figures

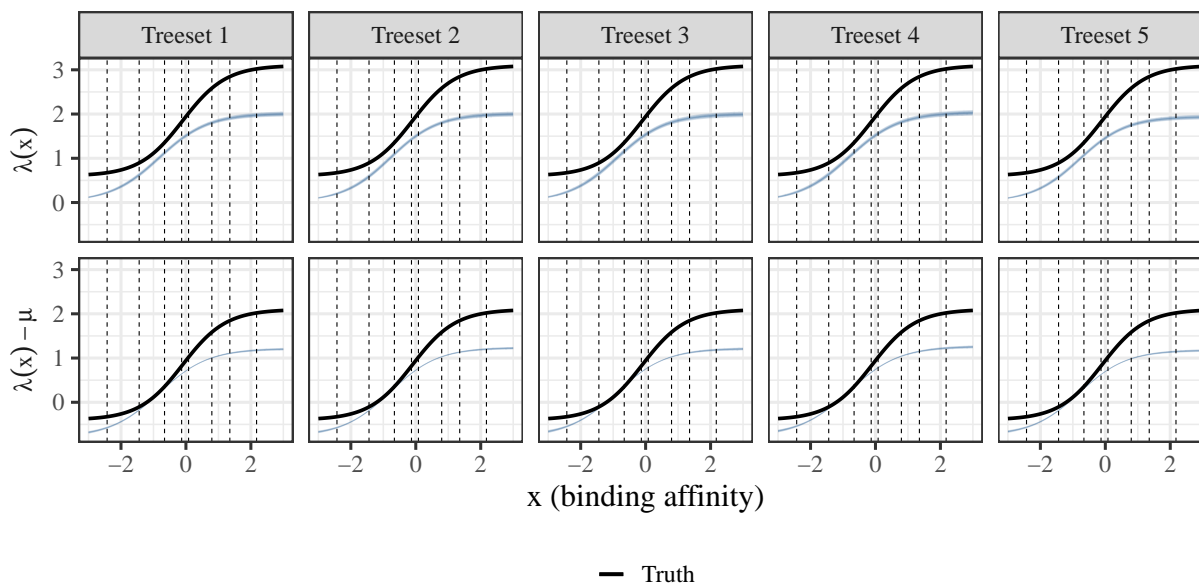


Figure 20: **(Soft carrying capacity)** Posteriors of the birth rate sigmoid and difference in birth rate and death rate, for each tree set. Shaded regions represent credible intervals (the widest being 90%). The dashed lines show the values of the type space, i.e. the points at which the birth rate sigmoid is inferred.

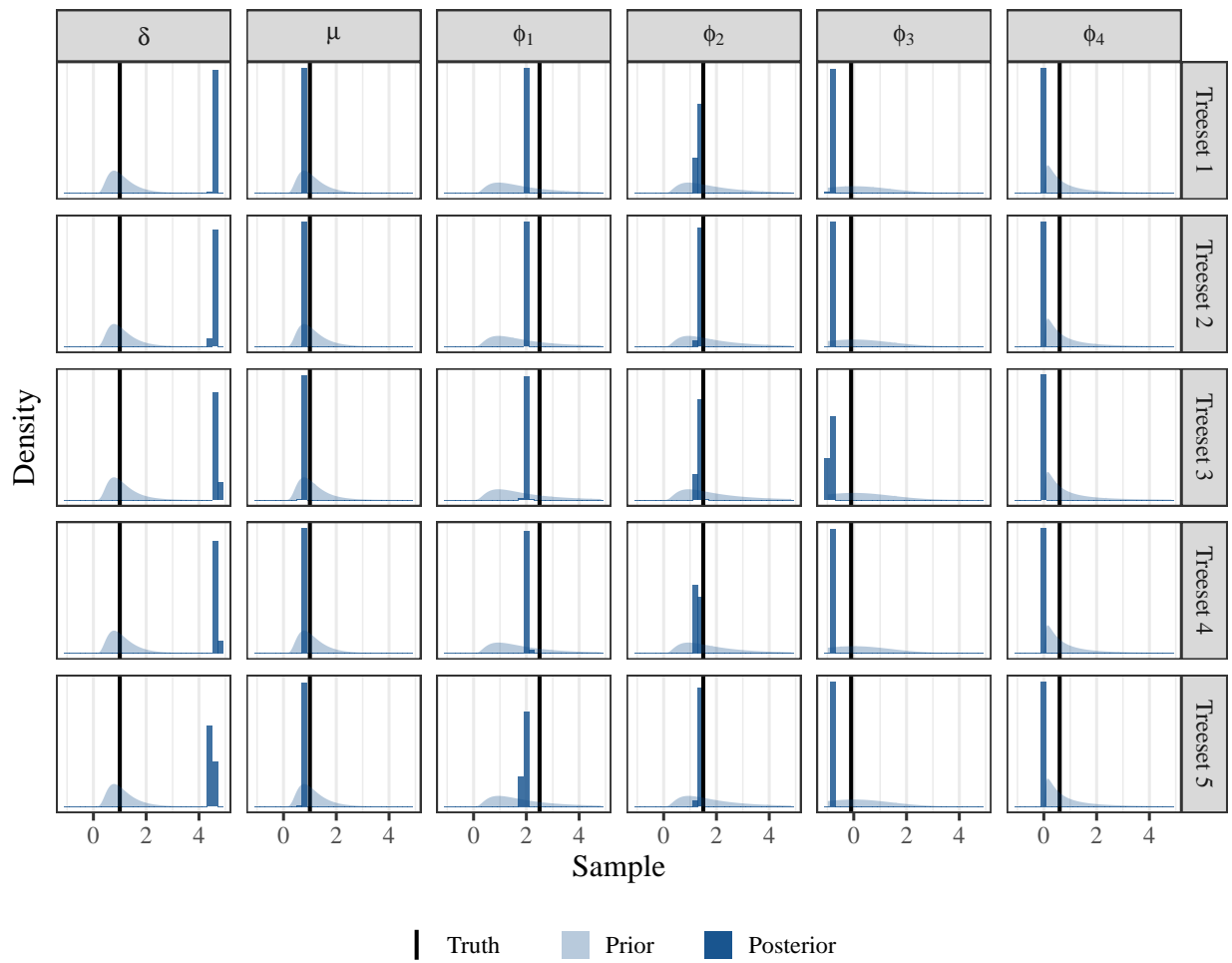


Figure 21: **(Soft carrying capacity)** Posterior histograms and prior density curves of each parameter, for each tree set.

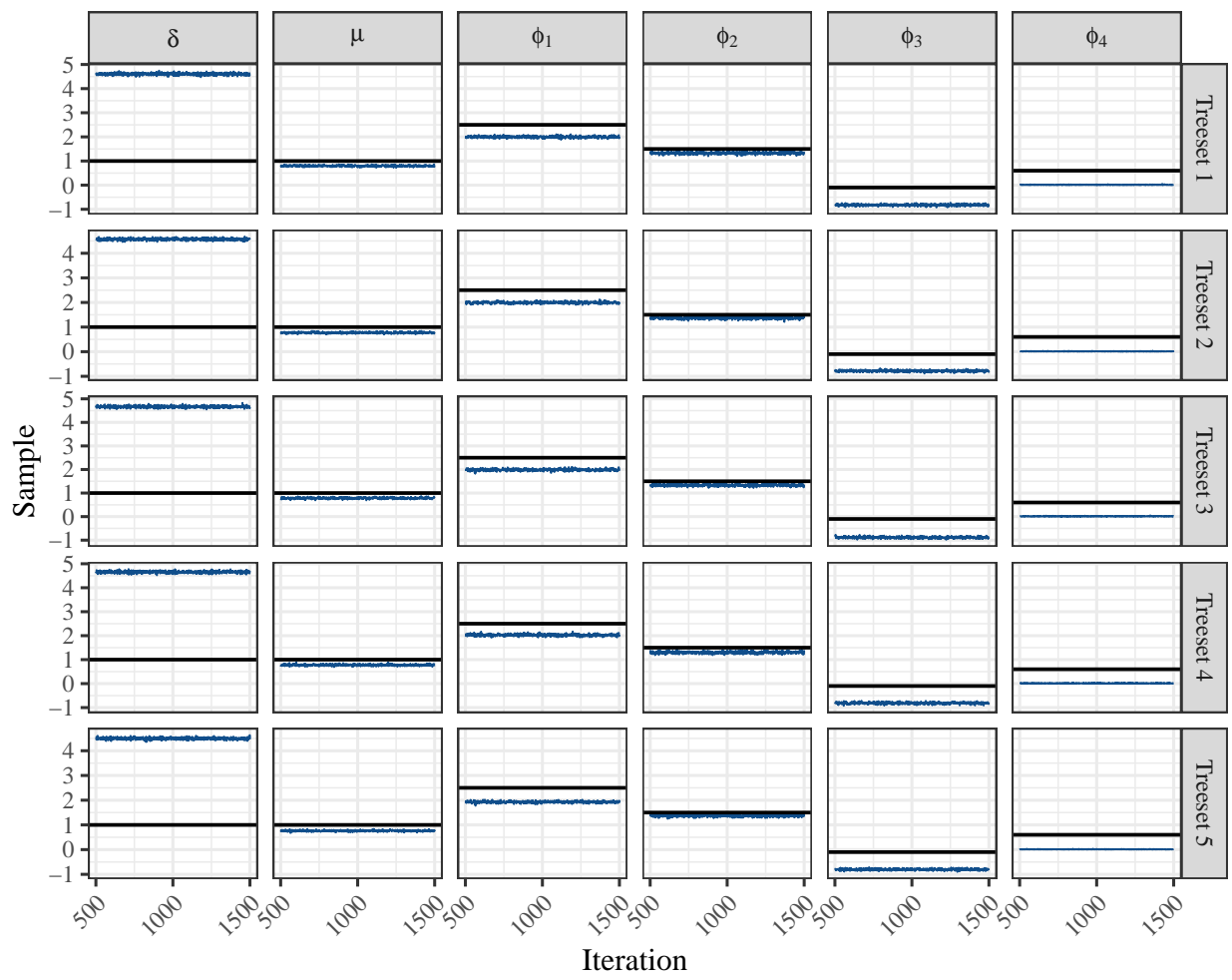


Figure 22: (Soft carrying capacity) Posterior traceplots of each parameter, for each tree set.

Carrying capacity with sequence-level mutation process

The following parameter values and figures correspond to the simulation study described in Section *Birth rate recovery, carrying capacity with sequence-level mutation process*.

Ground truth parameter values

- $\phi = [2.5, 1.5, -0.1, 0.6]$
- $\mu = 1$
- $\rho = 0.1$

The carrying capacity is set to be 1000.

Additional figures

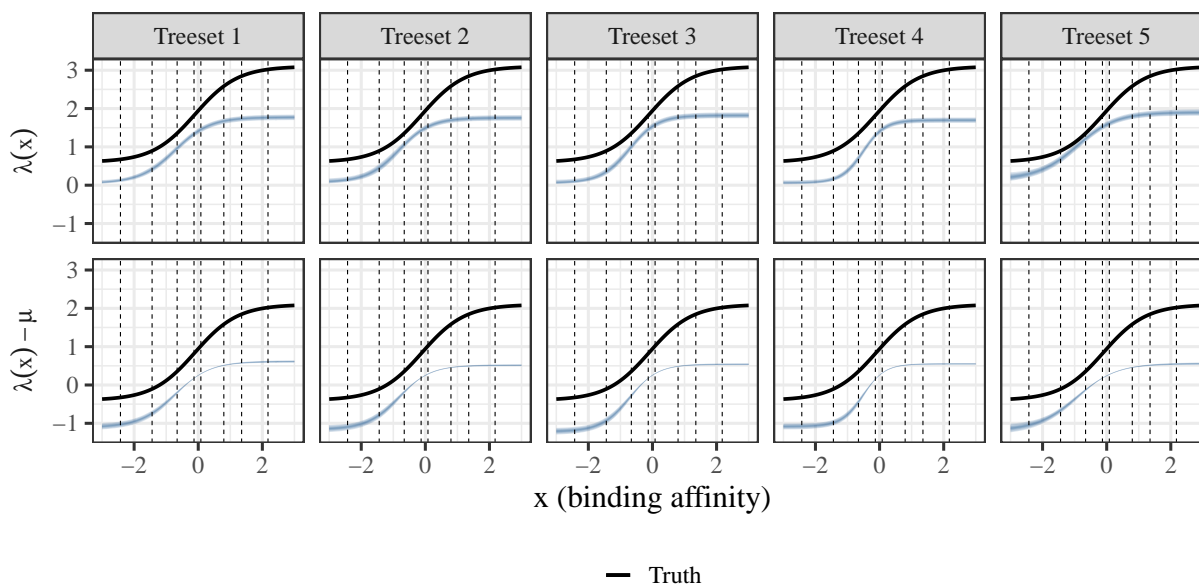


Figure 23: (**Carrying capacity with sequence-level mutation process**) Posteriors of the birth rate sigmoid and difference in birth rate and death rate, for each tree set. Shaded regions represent credible intervals (the widest being 90%). The dashed lines show the values of the type space, i.e. the points at which the birth rate sigmoid is inferred.

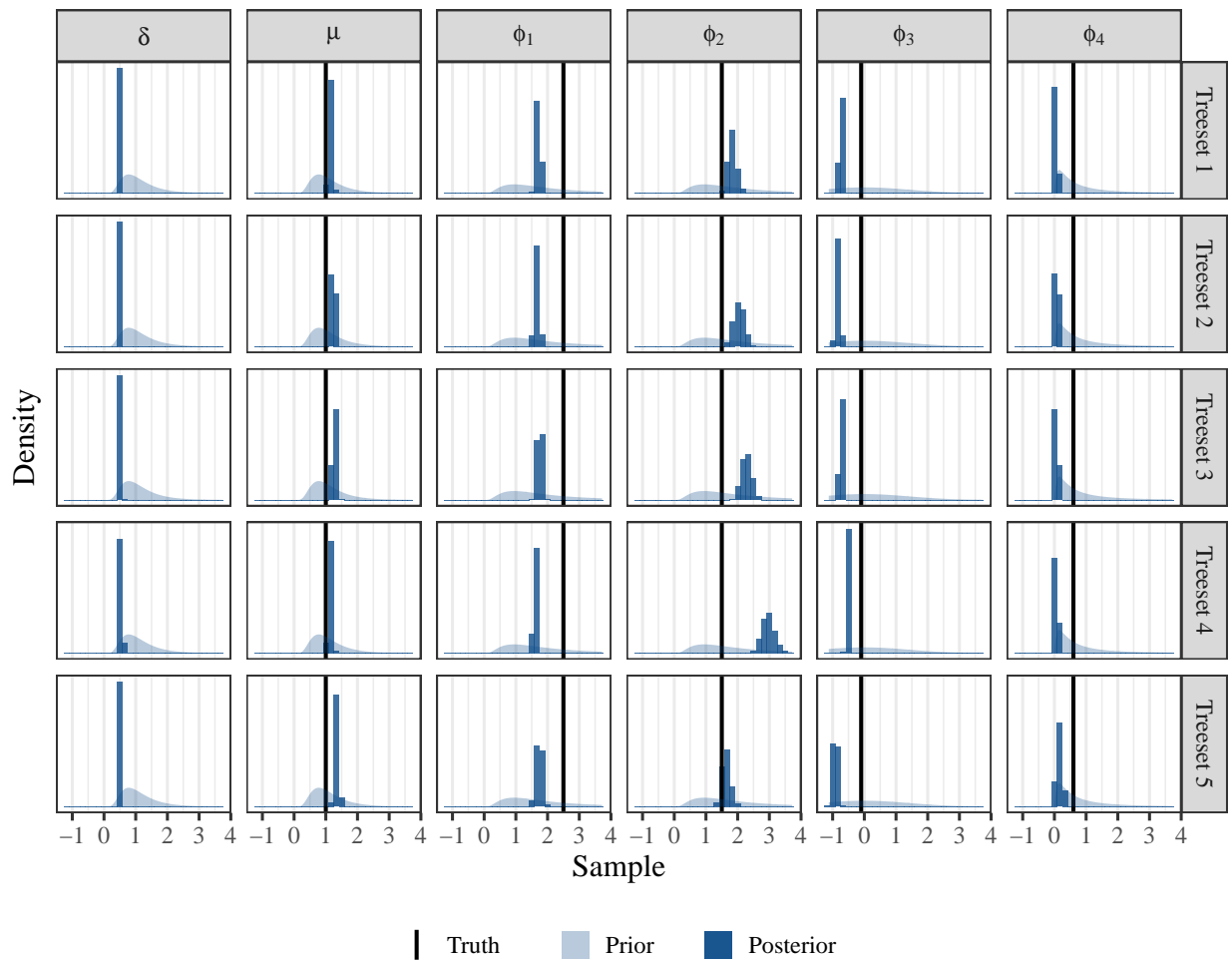


Figure 24: **(Carrying capacity with sequence-level mutation process)** Posterior histograms and prior density curves of each parameter, for each tree set.

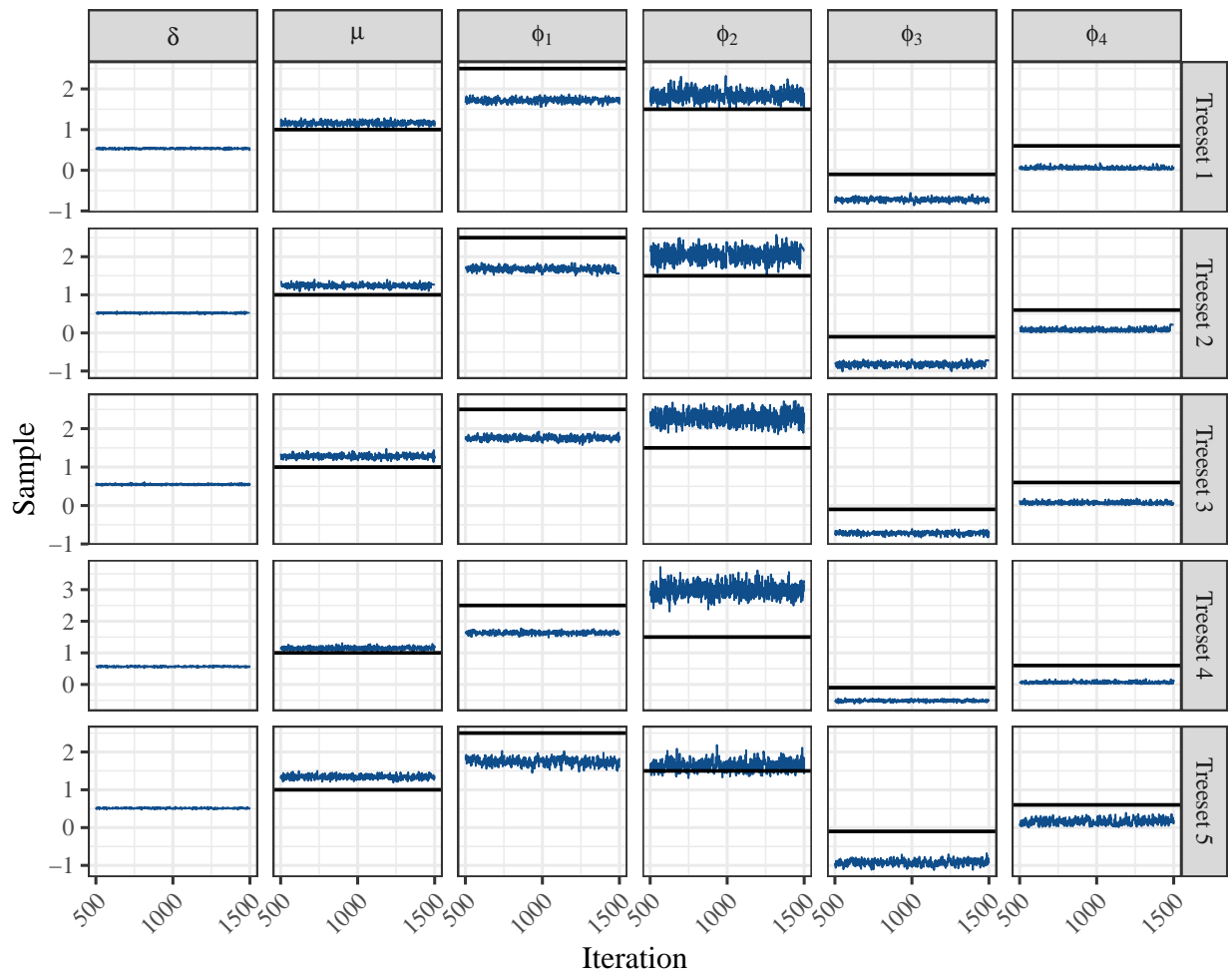


Figure 25: (Carrying capacity with sequence-level mutation process) Posterior traceplots of each parameter, for each tree set.

Additional data analysis figures

The following figures correspond to the data analysis described in Section *Analysis of experimental data*. To better understand the effect of phylogenetic uncertainty on our inference, we inferred posteriors for five tree sets, where each tree set was created by uniformly randomly selecting one tree from the BEAST chains for each germinal center (see Section *Data description*). The first figure visualizes the posterior over sigmoid curves inferred for each tree set. The second figure decomposes this posterior visualization into posterior histograms for each sigmoid parameter individually, as well as for the other branching process parameters. The third figure shows traceplots for each of these parameters. The final figure shows diagnostics of the posterior predictive distribution obtained when combining the inferences for each tree set.

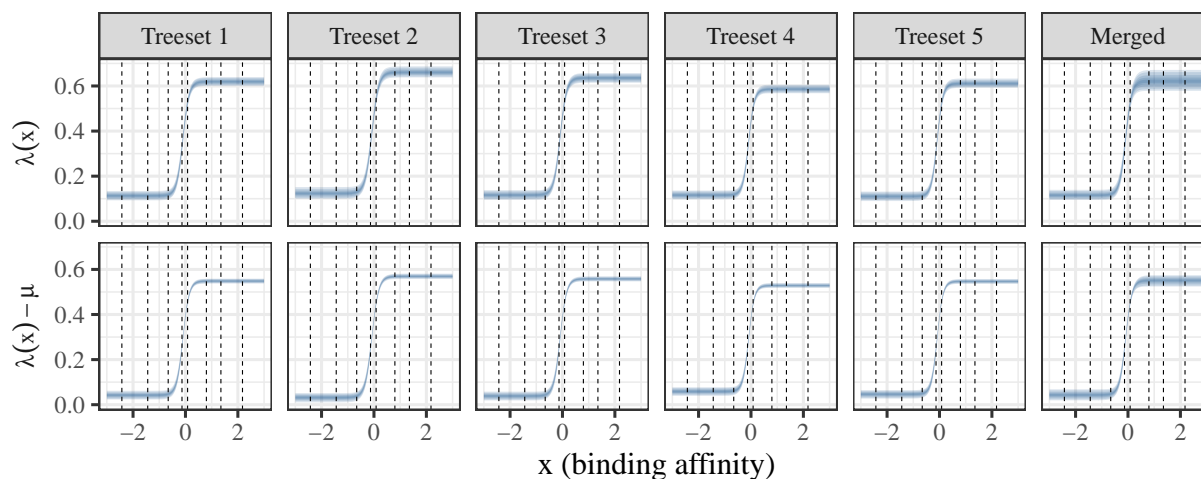


Figure 26: **(Data analysis)** Posteriors of the birth rate sigmoid and difference in birth rate and death rate, for each tree set. The last column displays the concatenation of the other five Markov chains, to illuminate the uncertainty we may not be capturing by using only one tree per germinal center to form our tree sets.

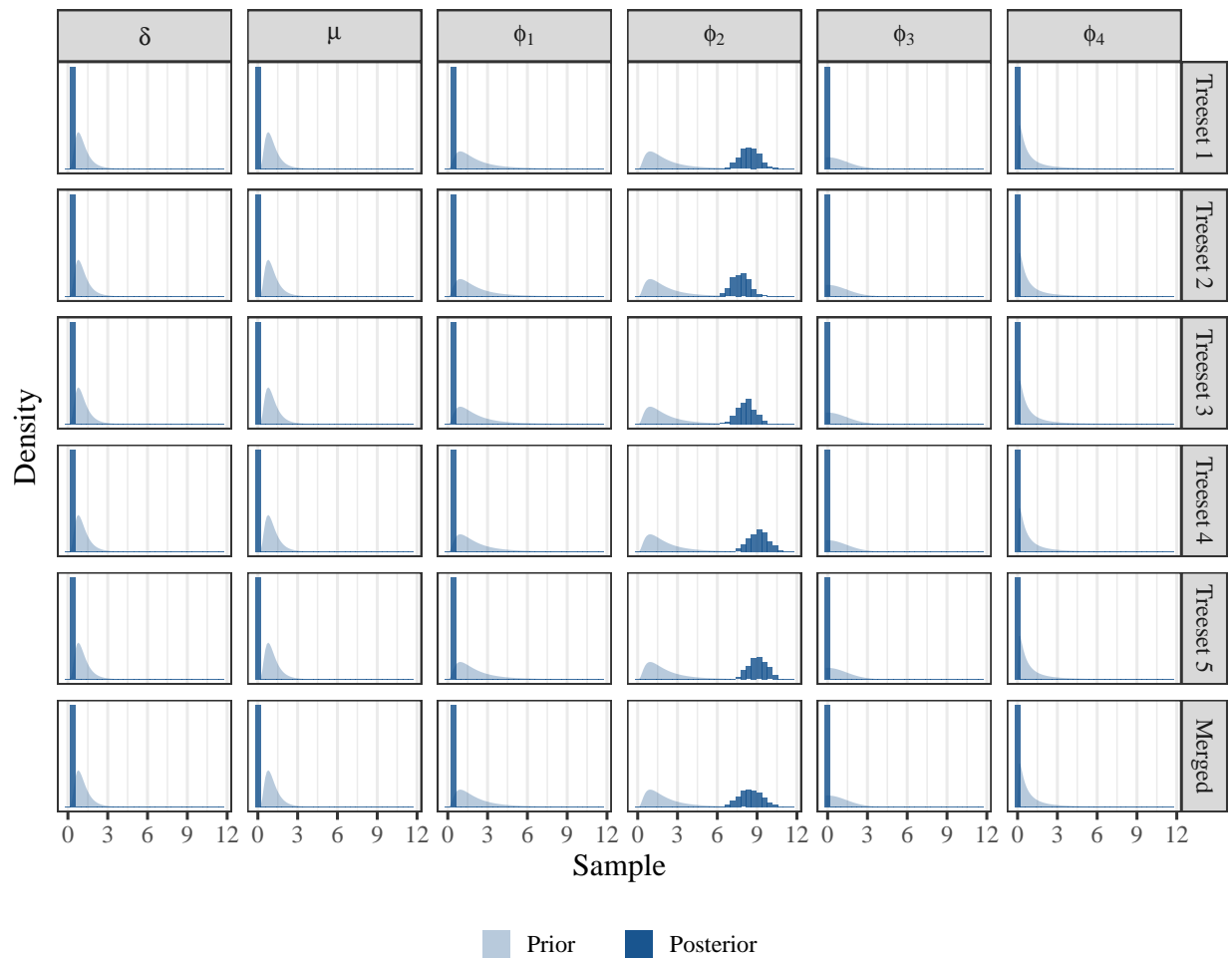


Figure 27: **(Data analysis)** Posterior histograms and prior density curves of each parameter, for each tree set.

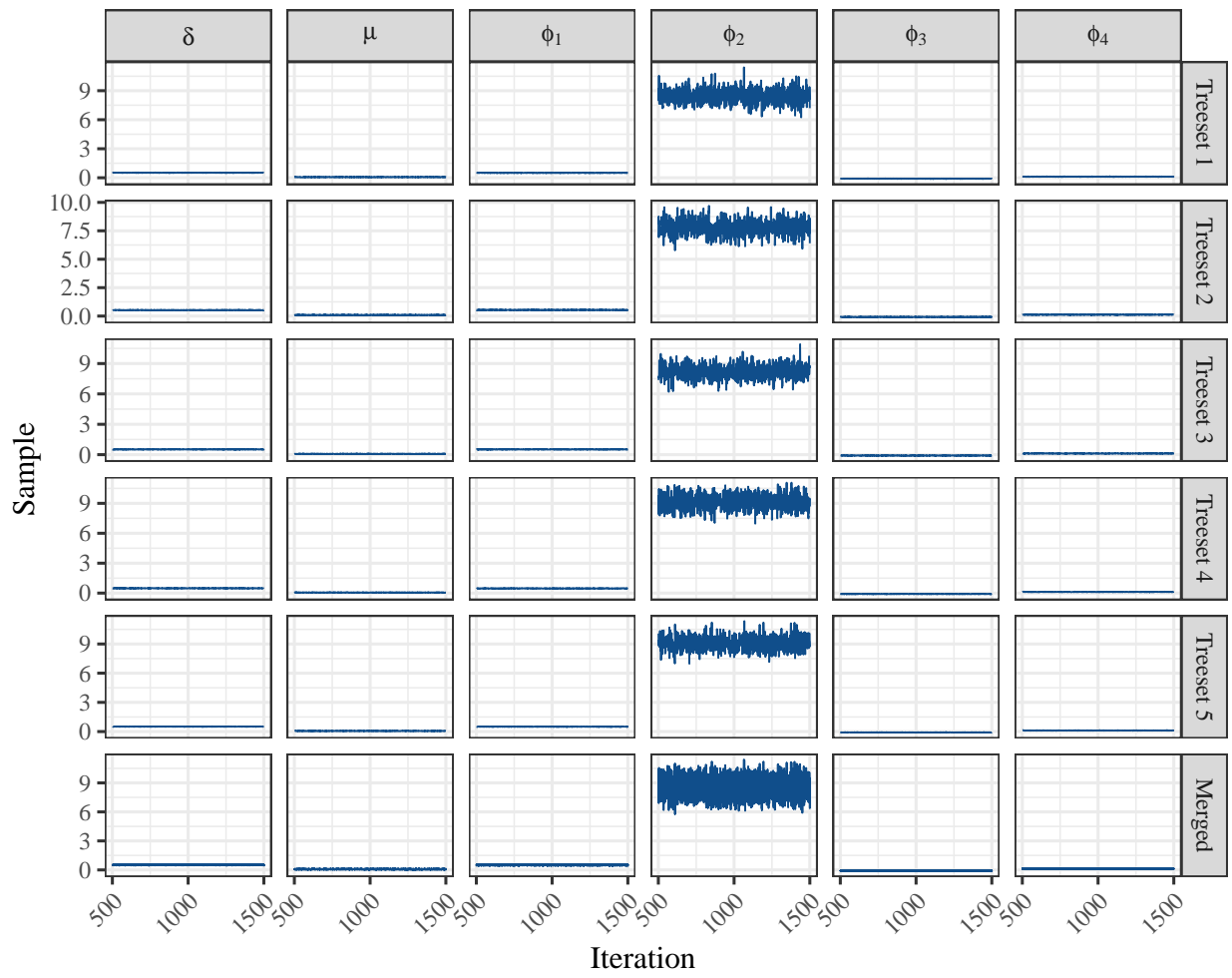


Figure 28: (Data analysis) Posterior traceplots of each parameter, for each tree set.

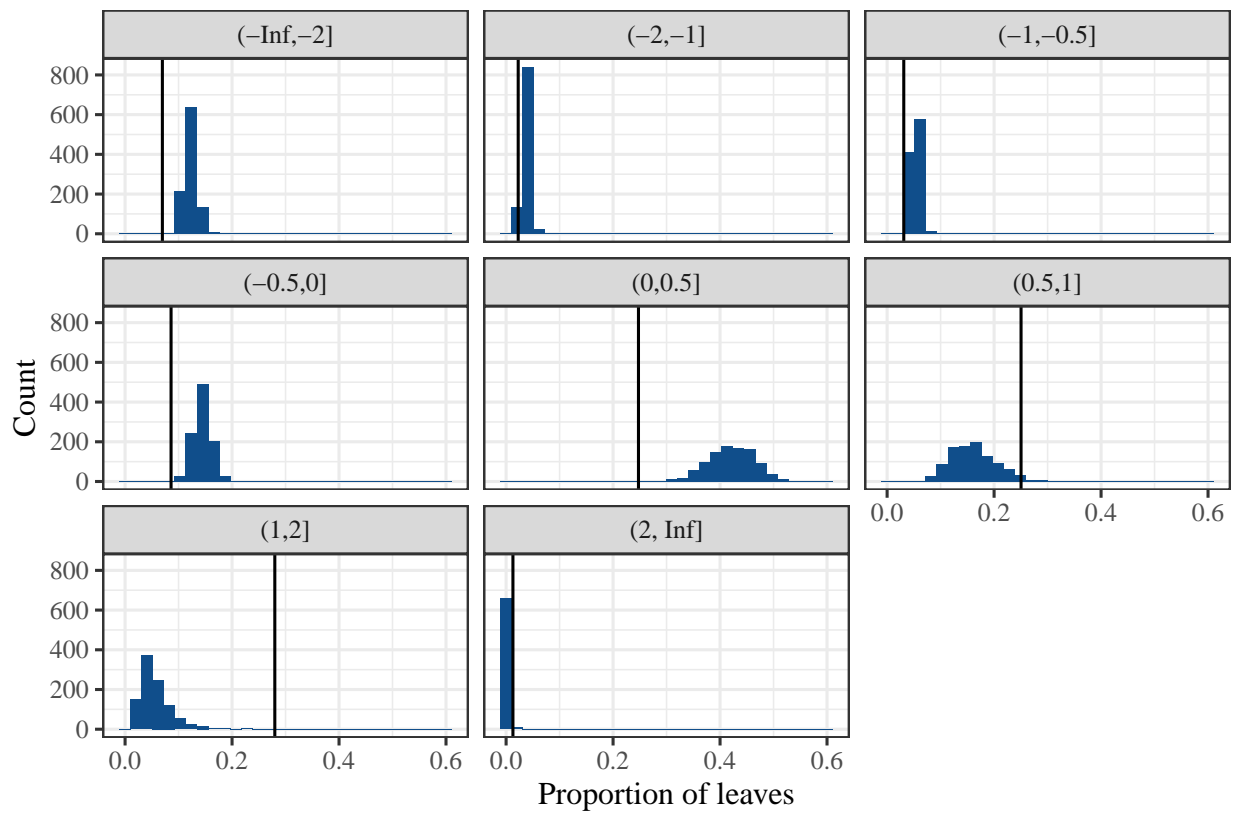


Figure 29: **(Data analysis)** Posterior predictive diagnostics. Histograms capture the distribution of the proportion of leaves in each affinity bin, over replicates produced by each posterior sample across all tree sets. Black vertical lines show the proportion of leaves with each affinity value observed in the experimental data.

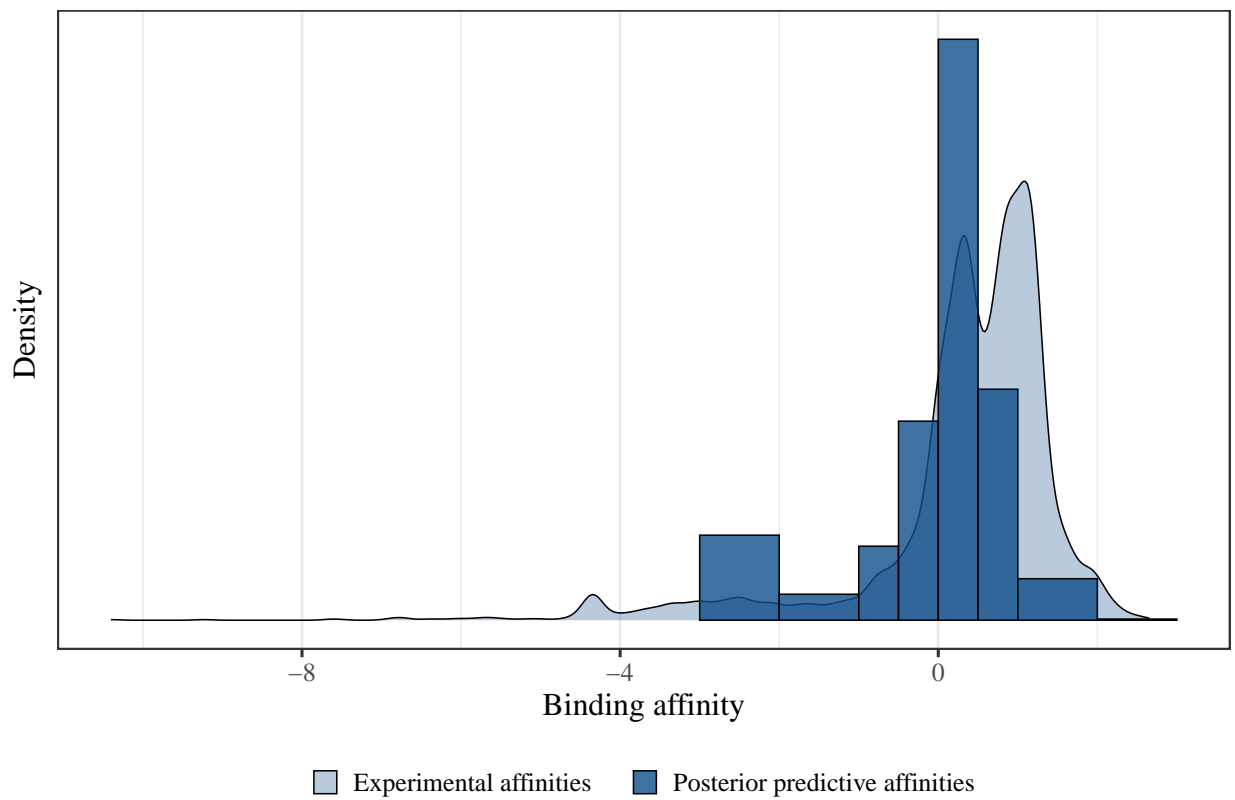


Figure 30: **(Data analysis)** Posterior predictive affinity distribution. The histogram captures the distribution of leaf affinities over replicates produced by each posterior sample across all tree sets. The density curve captures the distribution of leaf affinities observed in the experimental data. Note that this curve differs from the one drawn in Fig 4, which captures both leaf and internal nodes.

Priors

Parameter	Prior
ϕ_1	log-normal(0.5, 0.75)
ϕ_2	log-normal(0.5, 0.75)
ϕ_3	normal(0, 2)
ϕ_4	log-normal(-0.5, 1.2)
μ	log-normal(0, 0.5)
δ	log-normal(0, 0.5)

Table 1: Priors used in data analysis and simulation studies. The log-normal distributions are parameterized in terms of scale, and the normal distribution is parameterized in terms of variance.